

Homogenization-based design of microstructured membranes: wake flows past permeable shells

Pier Giuseppe Ledda¹ †, E. Boujo¹, S. Camarri², F. Gallaire¹, G. A. Zampogna¹

¹Laboratory of Fluid Mechanics and Instabilities, École Polytechnique Fédérale de Lausanne, CH-1015 Lausanne, Switzerland,

²Dipartimento di Ingegneria Civile e Industriale, Università degli Studi di Pisa, Pisa, Italy

(Received xx; revised xx; accepted xx)

A formal framework to characterize and control/optimize the flow past permeable membranes by means of a homogenization approach is proposed and applied to the wake flow past a permeable cylindrical shell. From a macroscopic viewpoint, a Navier-like effective stress jump condition is employed to model the presence of the membrane, in which the normal and tangential velocities at the membrane are respectively proportional to the so-called filtrability and slip numbers multiplied by the stresses. Regarding the particular geometry considered here, a characterization of the steady flow for several combinations of constant filtrability and slip numbers shows that the flow morphology is dominantly influenced by the filtrability and exhibits a recirculation region that moves downstream of the body and eventually disappears as this number increases. A linear stability analysis further shows the suppression of vortex shedding as long as large values of the filtrability number are employed. In the control/optimization phase, specific objectives for the macroscopic flow are formulated by adjoint methods. A homogenization-based inverse procedure is proposed to obtain the optimal constrained microscopic geometry from macroscopic objectives, which accounts for fast variations of the filtrability and slip profiles along the membrane. As a test case for the proposed design methodology, the cylindrical membrane is designed to maximize the resulting drag coefficient.

Key words:

MSC Codes (*Optional*) Please enter your MSC Codes here

1. Introduction

The behavior of wake flows past permeable bodies and membranes is of considerable interest owing to its large range of applications, both in nature and engineering. Several insects, as thrips and wasps, present bristled wings, offering a considerable aerodynamic benefit when compared to impervious wings in terms of propulsion efficiency per unit weight of the wing itself (Ellington 1980; Barta & Weihs 2006; Jones *et al.* 2016). Owls are renowned for their silent flight, which stems from the particular microscopic permeable structure of the hair composing the wings (Wagner *et al.* 2017; Jaworski & Peake 2020). The dandelion seeds are transported in the air by a structure called pappus, which behaves as a parachute. The presence of voids drastically decreases the falling velocity and stabilizes the steady

† Email address for correspondence: pier.ledda@epfl.ch

37 flow (Cummins *et al.* 2018; Ledda *et al.* 2019). At smaller scales, thin permeable shells are
38 of essential importance for unicellular organisms as a key point in their displacement and
39 feeding strategies (Asadzadeh *et al.* 2019). Within the vascular system of plants, permeable
40 microstructures called sieve plates are crucial for sap translocation (Jensen *et al.* 2016).

41 Besides these natural examples, there are several industrial applications concerning flows
42 through permeable structures with a plethora of microscopic properties and pore sizes,
43 ranging from millimeters for particle filtration to nanometers for desalination (Fritzmann
44 *et al.* 2007; Elimelech & Phillip 2011; Matin *et al.* 2011) and wastewater recovery (Shannon
45 *et al.* 2008; Rahardianto *et al.* 2010). At larger scales, the flow around permeable bluff bodies,
46 as parachutes and nets, is gaining more and more interest (Cummins *et al.* 2018; Labbé &
47 Duprat 2019). Fog water harvesting systems, particularly employed in arid climates (Olivier
48 2004; Labbé & Duprat 2019), are built using either nets (Park *et al.* 2013) or harps (Shi *et al.*
49 2018; Labbé & Duprat 2019).

50 In these last examples, a deep understanding of aerodynamic flows investing permeable
51 structures is crucial and, for decades, the uniform flow past a solid or porous circular cylinder
52 has been the testing ground to train the understanding of flows around bluff bodies. The
53 flow past a solid circular cylinder is steady for low values of the Reynolds number. The
54 steadiness of the wake is broken at a critical Reynolds number of 46.7 (Jackson 1987;
55 Provansal *et al.* 1987), beyond which the flow undergoes an instability that leads to a
56 two-dimensional oscillatory flow characterized by the alternate shedding of vortices, i.e.
57 the renowned von Kármán vortex street (Williamson 1996). At larger Reynolds numbers
58 $Re \approx 192$, the two-dimensional wake becomes unstable and three-dimensional structures
59 develop, whose characteristic trace is still the two-dimensional alternate shedding of vortices
60 (Barkley & Henderson 1996). The sequence of bifurcations that a flow may encounter can
61 be approached in the context of bifurcation theory and linear stability analysis (Chomaz
62 2005; Theofilis 2011). These methods are now largely employed and their reliability in the
63 prediction of instability thresholds and shedding frequencies close to the threshold (Barkley
64 2006) is now well assessed, spanning different length scales, from microfluidics systems
65 (Bongarzone *et al.* 2021), to bluff body aerodynamics (Meliga *et al.* 2009) and industrial
66 applications such as wind and hydraulic turbines (Jungo *et al.* 2013; Viola *et al.* 2014; Pasche
67 *et al.* 2017).

68 A largely investigated field in fluid dynamics is the control of the flow instabilities. One of
69 the first studies on the control of the von Kármán vortex street via modifications of the solid
70 surface and velocity can be traced back to Prandtl, who controlled the flow past a circular
71 cylinder using the blowing effect of a small hole on the surface (Willert *et al.* 2019). Castro
72 (1971) studied experimentally the flow around perforated flat plates for Reynolds numbers
73 of order 10^4 , finding that the vortex shedding was inhibited if the voids-to-material ratio
74 (porosity) is sufficiently large. Two different regimes were distinguished: a solid behavior
75 in which the von Kármán vortex street is present, with a downstream displacement of the
76 mean recirculation region and the vortices formation region, and a regime in which the
77 vortex shedding is quenched. Zong & Nepf (2012) performed an experimental study on
78 circular cylinders composed of arrays of smaller cylinders, for Reynolds numbers of order
79 10^4 , showing that also in this case the von Kármán vortex street was inhibited for large
80 porosities, with results similar to those of the numerical study of Nicolle & Eames (2011).
81 Recently, Steiros & Hultmark (2018) developed a theoretical framework to evaluate the drag
82 coefficient behavior for flat perforated plates, for Reynolds numbers of the order of 10^3 . In
83 a similar investigation for circular perforated plates, Steiros *et al.* (2020) also showed how
84 variable distributions of holes may strongly modify the flow morphology and the resulting
85 aerodynamic forces. Other analytical investigations on the aerodynamic forces on porous
86 airfoil have been performed in Hajian & Jaworski (2017) and Baddoo *et al.* (2021). In

87 Hajian & Jaworski (2017) a potential flow model to evaluate the aerodynamic forces on
88 thin permeable airfoils was proposed. The presence of a porous structure was described
89 by a seepage flow rate through the permeable surface. Baddoo *et al.* (2021) generalized
90 this analysis to the unsteady case such as pitching and heaving motion or gust loads. Other
91 experimental investigations focused on the drag variation of porous disks at low Reynolds
92 numbers (Strong *et al.* 2019) and on the fluid-structure interaction of porous flexible strips
93 (Pezzulla *et al.* 2020), to name a few. Ledda *et al.* (2018) performed a study on the effect
94 of the permeability on the stability of the steady and two-dimensional flow around porous
95 rectangles, obtaining a general permeability threshold beyond which the wake is steady.

96 In the works cited above, two essentially different ways to model porous structures can
97 be distinguished. Pore-scale models should be preferred for their high reliability (Icardi
98 *et al.* 2014; Crabill *et al.* 2018), but have the inconvenience of being very expensive from a
99 computational point of view, especially when one needs to characterize the flow with respect
100 to variations of the pore properties. An alternative to expensive pore-scale simulations is
101 the use of averaged models like Darcy equation (Darcy 1856) or its Brinkman extension
102 (Brinkman 1949). These models are computationally less expensive than their full-scale
103 counterparts and allow one to find a solution that is equivalent to the full-scale solution in an
104 averaged sense. However, one of their limitations resides in the presence of free parameters,
105 such as the permeability, which depend on the microscopic properties of the structure. While
106 these parameters were *a priori* unknown in the seminal work of Darcy, we are now able,
107 thanks to multi-scale techniques such as homogenization (Hornung 1997), to determine the
108 values of the parameters from the solution of closure pore-scale problems. For this reason,
109 homogenization provided relevant insights towards the modeling of multiscale fluid-structure
110 interactions, extending the classical Darcy model to treat inertia within the pores (Zampogna
111 & Bottaro 2016; Zampogna *et al.* 2016) and handling with interfaces between porous and
112 free-fluid regions (Lācis & Bagheri 2017; Lācis *et al.* 2017; Lācis *et al.* 2020). In Zampogna
113 & Gallaire (2020) homogenization revealed itself as a suitable tool to describe flows around
114 inhomogeneous microstructured permeable surfaces or membranes, opening the path to a
115 more formal approach in the characterization and design of membranes and filters.

116 The flow modifications induced by permeable membranes may find several applications.
117 As mentioned above, the dandelion pappus, which can be modeled as a permeable membrane,
118 shows values of the drag coefficient larger than if the pappus was completely impervious
119 (Cummins *et al.* 2018). Therefore, the modification of the permeability of a membrane is
120 a strategy to control and optimize the flow morphology. Lagrangian-based approaches are
121 one category of optimization procedures, which found large interest in the fluid dynamics
122 community, and are based on a variational formulation that allows one to compute gradients
123 at low cost through the use of the so-called adjoint variables (Luchini & Bottaro 2014).
124 Several studies were developed in a Lagrangian framework, as in the case of the sensitivity
125 to baseflow modifications (Marquet *et al.* 2008), steady forcing in the bulk (Boujo *et al.*
126 2013; Meliga *et al.* 2014) or at the solid walls by blowing and suction (Meliga *et al.* 2010;
127 Boujo & Gallaire 2014, 2015), for different objectives and flow configurations. Adjoint-
128 based sensitivity analysis tools can therefore be used as a building block for optimization
129 procedures, in steady (Camarri & Iollo 2010) and unsteady (Nemili *et al.* 2011; Lemke
130 *et al.* 2014) configurations. In Schulze & Sesterhenn (2013) an adjoint-based optimization
131 procedure to obtain the optimal permeability distribution for trailing-edge noise reduction
132 was proposed, in which the porous medium was modeled via the Darcy law.

133 Despite the increasing interest for multi-scale structures in fluid mechanics, systematic
134 approaches for the homogenization-based design and optimization of permeable membranes
135 are still lacking. In the present work, we aim to bridge this gap by linking the obtained
136 optimal profile of permeability to a real, realistic, full-scale structure (that can be eventually

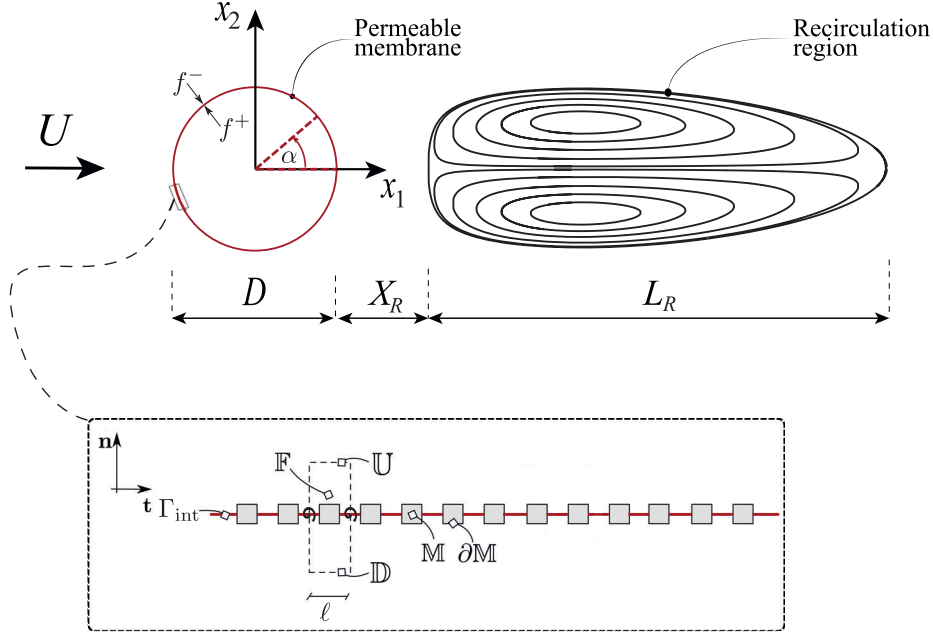


Figure 1: Top panel: fluid flow configuration considered in the present work and its typical structure past the cylindrical permeable shell (Γ_{int} , in red) of diameter D , where we denoted the length of the recirculation region L_R and its distance X_R from the rear of the body. The angle α is measured counterclockwise starting from the rear. The superscript \cdot^- indicates that the generic variable f is evaluated in the outer fluid region while the superscript \cdot^+ refers to the inner fluid region. Bottom panel: zoom on the shell to highlight its microscopic structure in cylindrical coordinates, made by replication of solid inclusions denoted by \mathbb{M} with boundary $\partial\mathbb{M}$ and sketch of the elementary unit cell in dashed line, whose tangential-to-the-surface size is ℓ . The fluid domain within the unit cell is denoted by \mathbb{F} while its upper and lower boundaries are indicated respectively with \mathbb{U} and \mathbb{D} .

137 built). For this purpose, we propose a formal framework for the optimization of permeable
 138 membranes, applying it to the particular case of wake flows in the low to moderate Reynolds
 139 numbers regime. We exploit the concepts of stability analysis, homogenization theory and
 140 gradient-based optimization so as to give a procedure to obtain the full-scale structure
 141 satisfying user-defined macroscopic flow objectives. The paper is structured as follows.
 142 In Section 2 we introduce the mathematical formulation of the problem and describe the
 143 homogenization-based design procedure. We then apply the procedure by first studying, in
 144 Section 3, the steady solutions of the flow equations and their linear stability with respect
 145 to infinitesimal perturbations. Section 4 is devoted to the geometric reconstruction of the
 146 microscopic geometry for salient cases and to the comparison with the homogenized model.
 147 In Section 5, we then move to a gradient-based optimization of a membrane with variable
 148 properties, and in Section 6, using a homogenization-based inverse procedure, we retrieve
 149 the full-scale geometry of the considered membrane from the optimal properties found in
 150 Section 5 and eventually compare the properties of the full-scale structure to those predicted
 151 by the homogenized model.

152 2. A formal framework to support the design of microstructured permeable 153 surfaces

154 In this section, we introduce the main physical hypotheses, strategy and tools to aid the design
 155 of microstructured membranes in order to tune their aero- and hydro-dynamics properties.

2.1. Problem formulation and model description

156

157 We consider a two-dimensional permeable cylindrical shell of diameter D subject to an
 158 incompressible flow of a Newtonian fluid of constant density ρ and viscosity μ , whose
 159 free-stream velocity is U , as depicted in figure 1. The cylindrical shell is constituted by a
 160 mono-disperse repetition of solid inclusions, whose characteristic length scale is denoted
 161 as ℓ . Since $\ell \ll D$ we can introduce a separation of scales parameter defined as the ratio
 162 between the two length scales at play:

163

$$\varepsilon := \frac{\ell}{D} \ll 1. \quad (2.1)$$

164

165 Under this assumption, a homogenized model is employed to describe the flow through the
 166 membrane (Zampogna & Gallaire 2020), which is macroscopically represented by a smooth
 167 surface with zero thickness. In the outer and inner pure-fluid regions splitted by the permeable
 168 shell, the incompressible Navier-Stokes equations hold. The velocity \mathbf{u}^* and pressure p^*
 169 fields are introduced, where the superscript $*$ denotes dimensional variables. Introducing the
 Cartesian coordinate system (x_1, x_2) (figure 2), these equations read ($i, j = 1, 2$):

170

$$\begin{aligned} \rho \partial_i^* u_i^* + \rho u_j^* \partial_j^* u_i^* &= -\partial_i^* p^* + \mu \delta_{jj}^{*2} u_i^*, \\ \partial_i^* u_i^* &= 0. \end{aligned} \quad (2.2)$$

171

172 The flow through the membrane is described by an effective stress jump model, consisting of
 173 the discontinuity in the fluid stress and the continuity of velocity across the permeable shell,
 174 denoted here with Γ_{int} (red line in figure 1). Labelling with the superscript $-$ and $+$ variables
 175 evaluated respectively in the outer and inner fluid regions, as shown in figure 1, the interface
 conditions at the membrane Γ_{int} read ($i, j, k = 1, 2$)

176

$$\begin{aligned} u_i^* &= u_i^{*+} = u_i^{*-} \\ u_i^* &= \frac{\ell}{\mu} M_{ij} \left(\Sigma_{jk}^* (p^{*-}, \mathbf{u}^{*-}) - \Sigma_{jk}^* (p^{*+}, \mathbf{u}^{*+}) \right) n_k \end{aligned} \quad (2.3)$$

177

where Σ_{jk}^* is the jk -th component of the stress tensor defined as

178

$$\Sigma_{jk}^* (p^*, \mathbf{u}^*) = -p^* \delta_{jk} + \mu (\partial_j^* u_k^* + \partial_k^* u_j^*), \quad (2.4)$$

179

and the components of the tensor M_{ij} (figure 1) are

180

$$M_{ij} = \bar{L}_t t_i t_j - \bar{F}_n n_i n_j, \quad (2.5)$$

181

182 where \bar{L}_t , \bar{F}_n are evaluated by solving microscopic problems within the elementary unit cell
 183 introduced in figure 1, in the local reference frame $(\mathbf{t}, \mathbf{n}) = ((-\sin(\alpha), \cos(\alpha)), (\cos(\alpha), \sin(\alpha)))$
 184 (cf. Zampogna & Gallaire 2020, and Section 4.2 for a detailed description of these problems
 185 and their solution). We note that the generic tensor N_{ij} of the original condition developed
 186 in Zampogna & Gallaire (2020) is replaced here by $-M_{ij}$ since, in the present work, we
 187 consider only solid inclusions which are symmetric with respect to Γ_{int} and we assume that
 inertia is negligible within the pores.

188

By considering D and U respectively as reference length and velocity scales, we obtain
 189 the following system of non-dimensional equations:

190

$$\begin{aligned} \partial_t u_i + u_j \partial_j u_i &= -\partial_i p + \frac{1}{Re} \partial_{jj}^2 u_i \\ \partial_i u_i &= 0, \end{aligned} \quad (2.6)$$

191

where we introduced the Reynolds number as $Re = \frac{\rho U D}{\mu}$. The non-dimensional interface

192 condition on Γ_{int} reads:

$$193 \quad u_i = u_i^+ = u_i^- \quad (2.7)$$

$$194 \quad u_i = Re \mathcal{M}_{ij} (\Sigma_{jk}(p^-, \mathbf{u}^-) - \Sigma_{jk}(p^+, \mathbf{u}^+)) n_k,$$

$$195 \quad \Sigma_{jk}(p, \mathbf{u}) = -p\delta_{jk} + \frac{1}{Re}(\partial_j u_k + \partial_k u_j), \quad (2.8)$$

$$197 \quad \mathcal{M}_{ij} = \mathcal{L}t_i t_j - \mathcal{F}n_i n_j, \quad (2.9)$$

198 where $\mathcal{L} = \epsilon \bar{L}_t$ and $\mathcal{F} = \epsilon \bar{F}_n$ are respectively labelled as slip and filtrability numbers. The
 199 interface condition (2.7) thus states that the velocity at the membrane is proportional to
 200 the Reynolds number and to the tensor \mathcal{M}_{ij} . According to Zampogna & Gallaire (2020),
 201 the tensor \mathcal{M}_{ij} describes the geometry of the microscopic problem with negligible inertial
 202 effects within the microscopic domain, in an adimensionalization which makes the problem
 203 independent of the macroscopic Reynolds number. In the macroscopic perspective, the
 204 relative importance between inertial and viscous effects is taken into account by Re in
 205 equation (2.7). More specifically, the velocity locally tangential to the interface is proportional
 206 to \mathcal{L} , while the normal velocity is proportional to \mathcal{F} . Therefore, the filtrability and slip
 207 numbers denote the capability of the flow to pass through and slip along the membrane,
 208 respectively. Different limiting behaviors of the interface condition (2.7) are thus identified.
 209 When $\mathcal{F} = 0$, the flow cannot pass through the membrane but it can slip along it. This
 210 situation is analogous to the one outlined in Zampogna *et al.* (2019) for rough surfaces, and
 211 the resulting boundary condition is formally analogous to the so-called Navier-slip condition.
 212 When $\mathcal{L} = 0$, a no-slip condition is imposed on the tangential velocity, while the normal one
 213 varies in proportion to \mathcal{F} . This situation can be interpreted as an averaged Darcy law through
 214 the membrane, where the viscous effects and thus the slip at the interface are neglected
 215 (Zampogna & Bottaro 2016). Other limiting cases occur for $\mathcal{F} = 0$ and $\mathcal{L} = 0$, which
 216 corresponds to a solid wall condition, and for $\mathcal{F} \rightarrow \infty$ and $\mathcal{L} \rightarrow \infty$, which corresponds
 217 to the imposition of the continuity of stresses across the microscopic elementary volume
 218 whose size tends to zero, and thus to the absence of the solid structure. Since the flow
 219 configuration is solved numerically, we refer to the caption of figure 2 for an explanation
 220 of the boundary conditions imposed on the remaining boundaries of the computational
 221 domain. These conditions, in non-dimensional form, read $u_1 = 1$, $u_2 = 0$ at the inlet and
 222 $(-p\delta_{ij} + \frac{1}{Re}\partial_j u_i)n_j = 0$ on the lateral and outlet boundaries.

223 2.2. Homogenization-based design

224 In the existing literature, works on permeable bodies and membranes were focused on the
 225 evaluation of the macroscopic parameters of the membrane (slip and filtrability) starting from
 226 the microscopic geometry. Other works treated the above-mentioned macroscopic quantities
 227 as free parameters in order to characterize, modify and optimize the fluid flow surrounding the
 228 porous body, without providing an explicit link between these parameters and the microscopic
 229 structure of the membrane. Here, we propose to fill the gap between these two aspects by
 230 an *inverse* formulation of the homogenized model that on one hand is extremely efficient for
 231 parametric studies and on the other hand allows one to deduce the microscopic geometry
 232 which realizes given distributions of \mathcal{L} and \mathcal{F} .

233 The inverse formulation aims at deriving the microscopic characteristics of the membrane
 234 based on the macroscopic features of the steady flow. In the present paper, an efficient
 235 workflow to deduce full-scale structures starting from the homogenized model is adopted
 236 (cf. the top frame of figure 3). The generic workflow therefore firstly consists of an analysis
 237 where the homogenized model is employed. The implementation of the homogenized model
 238 implies a decoupling between the microscopic structure and the macroscopic effect on the

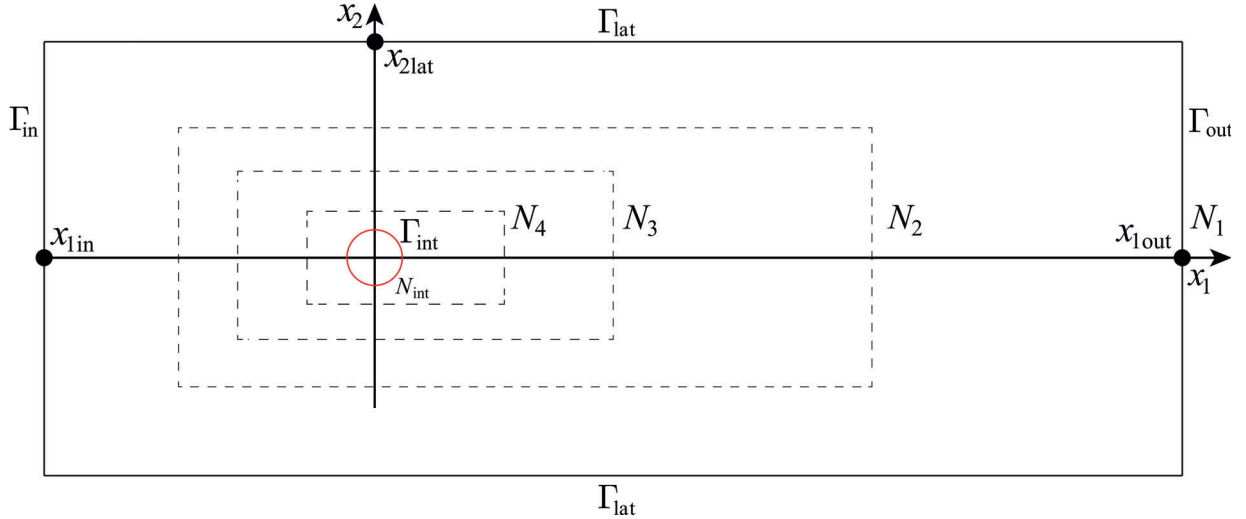


Figure 2: Computational domain considered in the present work. The regions denoted with N_j represent the different mesh refinements used when approaching the permeable shell. At the inlet Γ_{in} a free-stream condition with a Dirichlet boundary condition of the form $u_1^* = U$ and $u_2^* = 0$ is imposed, while on the lateral boundaries Γ_{lat} and at the outlet Γ_{out} the stress-free condition $(-p^* \delta_{ij} + \mu \partial_j^* u_i^*) n_j = 0$ is used. On the interface Γ_{int} conditions (2.3) are imposed.

239 flow. On the one hand, parametric studies and optimizations are simplified owing to the
 240 reduced number of parameters; on the other hand, the retrieval of the full-scale structure
 241 is performed in a second step, when the macroscopic feedback embodied in the scalar
 242 parameters of the homogenized model is already known.

243 For illustration purposes, the workflow is specialized to analyze the flow configuration
 244 shown in figure 1, leading to the following procedure:

245 • Using the homogenized approach described in the previous section, we perform a
 246 parametric study for varying \mathcal{L} and \mathcal{F} , by solving the steady version of equations (2.6-2.7)
 247 for different values of the Reynolds number.

248 • We characterize the topological properties of the steady flow (e.g. the characteristic
 249 dimensions of the recirculation region) and the aero/hydro-dynamics properties of the
 250 permeable shell as, for instance, its drag coefficient.

251 • The validity of the performed investigation, carried out assuming that the flow is steady,
 252 is verified by linear stability analysis (Chomaz 2005; Theofilis 2011). The latter has the
 253 advantage to characterize the stability of the steady solution with a computational cost
 254 comparable to that needed to compute steady solutions, thus making it suitable for the
 255 performed parametric study.

256 • Once the variety of possible steady solutions is reduced by excluding the unstable
 257 configurations, for which the steady analysis would be inappropriate, the objective to be
 258 optimized is defined, e.g. the maximum drag coefficient for a fixed Reynolds number.
 259 Therefore, the values of \mathcal{L} and \mathcal{F} that maximize the objective function are identified. This can
 260 be done by employing adjoint procedures for spatially-homogeneous membrane properties.
 261 However, since in this work we perform a parametric study, the values are directly deduced
 262 from the latter.

263 • We then move from the macroscopic perspective to the microscopic one, aiming
 264 at identifying the geometry of the membrane that corresponds in macroscopic terms to
 265 the optimal configuration previously identified. We therefore perform the microscopic
 266 simulations described in Zampogna & Gallaire (2020) for a fixed geometry by varying

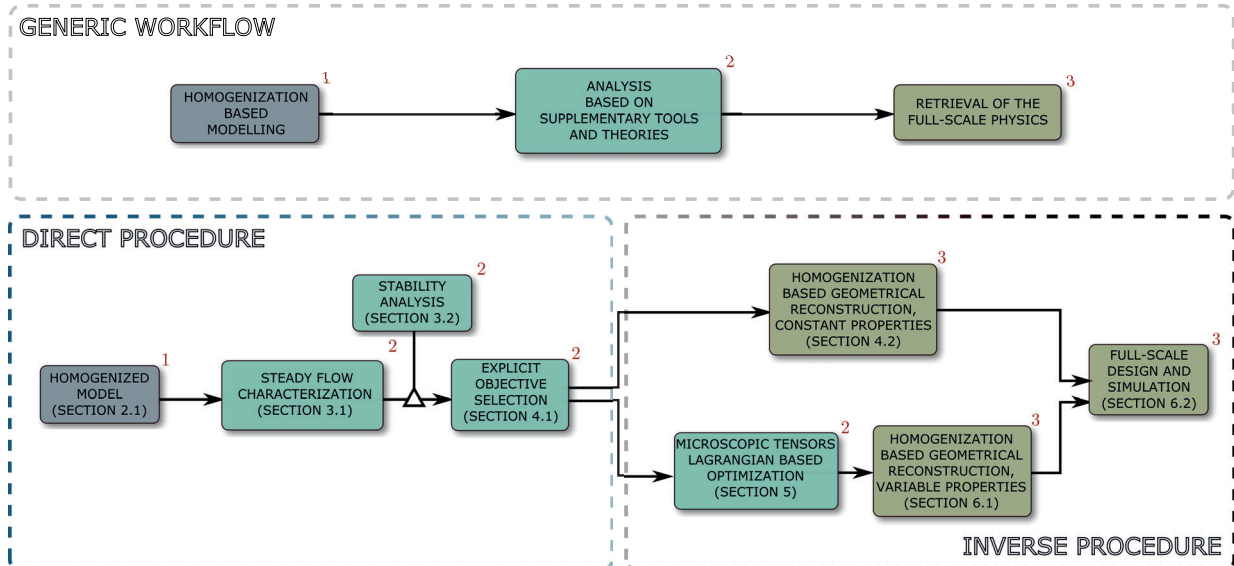


Figure 3: Top frame: generic workflow to efficiently analyze a flow configuration via homogenized models integrated in classical analyses like, for instance, parametric studies, stability analysis or adjoint-optimization finalized to identify configurations of interest. The retrieval of the full-scale physics for the identified configurations is done in a last step leading to a substantial reduction of the complexity of the optimization problem. Bottom frames: the generic workflow has been specialized in the present paper to design permeable membranes. Colors and red numbers are used to correctly place each step of the procedure adopted in the present paper in the generic workflow. A homogenized model is used to characterize a specific flow configuration in a *direct* formulation. This allows one to identify a set of objectives and the corresponding values of the macroscopic parameters realizing these objectives. Homogenization is then used in an *inverse* formulation to associate the values of the macroscopic tensors with a specific microscopic geometry.

267 the fluid-to-solid ratio of the porous shell. We thus define the microscopic geometrical
 268 parameters and ε .

269 • We eventually verify the accuracy of the resulting structure by comparing the full-scale
 270 simulations with the homogenized results.

271 The outlined technique has the great advantage to drastically reduce the complexity of the
 272 problem and give a parametric map of the properties of the flow by varying the microscopic
 273 geometry of the membrane. An extension of this technique to treat the case of a microscopic
 274 geometry that varies along the membrane is obtained by a gradient-based optimization
 275 implemented via a Lagrangian approach, detailed in Section 5.2. In particular, we consider as
 276 a starting point the configuration, with constant slip and filtrability numbers, that maximizes
 277 the drag coefficient. We evaluate the sensitivity of this predefined objective function (drag
 278 maximization) with respect to spatial inhomogeneities of the properties of the membrane and
 279 perform a gradient-based optimization. The resulting structure is then obtained by following
 280 an inverse procedure based on the microscopic calculations of Zampogna & Gallaire (2020),
 281 but extended to the case of variable properties along the membrane.

282 We finally underline that the procedure, illustrated here for the specific case of a wake
 283 flow, is of general validity and can thus be applied to a generic flow.

284 3. Case study: flow past a cylindrical porous shell

285 In this section, we report the results of the *direct* part of the procedure sketched in figure
 286 3, preparatory to the homogenization-based geometrical reconstruction and Lagrangian
 287 optimization, constituting the *inverse* part of the procedure. We characterize the steady

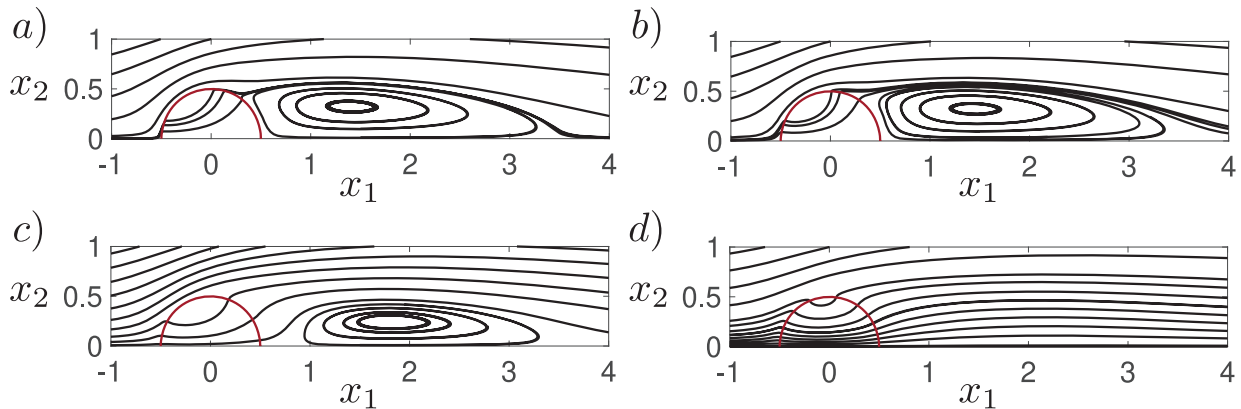


Figure 4: Streamlines of the flow past the cylindrical permeable shell at $Re = 50$ for $\mathcal{L} = 10^{-4}$ and four different values of \mathcal{F} : (a) $\mathcal{F} = 10^{-4}$, (b) $\mathcal{F} = 10^{-3}$, (c) $\mathcal{F} = 10^{-2}$, (d) $\mathcal{F} = 3 \times 10^{-2}$.

288 flow in terms of the recirculation region and drag coefficient, and then we move to the
 289 stability properties of the steady wake and the features of possible unsteady modes.

290 Equations (2.6) are numerically implemented via their weak formulation in the finite
 291 element solver COMSOL Multiphysics, using a domain decomposition method (cf. for
 292 instance Quarteroni 2017) to couple the outer and inner flow. In this framework, the
 293 macroscopic model (2.7) acts like an interface condition between two different fluid domains.
 294 In order to exchange information from the outer to the inner domain, the stress jump condition
 295 is implemented by exploiting the interface integral emerging from the weak formulation,
 296 while, to exchange information from the inner to the outer domain, the continuity of velocity
 297 is imposed via a Dirichlet boundary condition. We exploit the built-in solver for non-linear
 298 systems, based on a Newton algorithm. The spatial discretization is based on the Taylor–Hood
 299 (P2-P1) triangular elements. The unstructured grid is made of five different regions of
 300 refinement (figure 2), whose edge densities have been chosen after a convergence analysis
 301 reported in Appendix A.

302 The eigenvalue problems resulting from the linear stability analysis carried out in Section
 303 3.2 are solved with the COMSOL Multiphysics built-in eigenvalue solver, based on the
 304 ARPACK library; mesh convergence is checked also for this problem and it is reported in
 305 Appendix A.

306

3.1. Steady flow characterization

307 The steady wake past a circular solid cylinder is characterized by a recirculation region
 308 that is symmetric with respect to the x_1 -axis. We denote with (\mathbf{U}, P) the steady solution of
 309 equations (2.6). Since, by construction, we do not introduce any further asymmetry, also the
 310 flow past the permeable cylindrical shell is expected to be x_1 -symmetric. For this reason,
 311 we only report the flow field in the region $x_2 > 0$. For the present analysis, we introduce
 312 the length of the recirculation region L_R and its distance from the rear of the body X_R as
 313 defined in figure 1. In figure 4 we report the flow streamlines for different values of \mathcal{F} when
 314 $Re = 50$ and $\mathcal{L} = 10^{-4}$. At low values of \mathcal{F} , e.g. $\mathcal{F} = 10^{-4}$, the wake is similar to the solid
 315 case, i.e. characterized by a recirculation region attached to the rear of the cylinder ($X_R \approx 0$).
 316 As the value of \mathcal{F} increases, the recirculation region detaches from the body and moves
 317 downstream. A further increase in \mathcal{F} implies a size reduction of the recirculation region
 318 (L_R), and at very large values of \mathcal{F} , i.e. $\mathcal{F} = 3 \times 10^{-2}$, the recirculation region eventually
 319 disappears ($L_R = 0$).

320 In figure 5 we report the variation of the recirculation region with \mathcal{F} , for different slip
 321 numbers \mathcal{L} and for $Re = 50$. Independently of the value of the slip number, a behavior similar

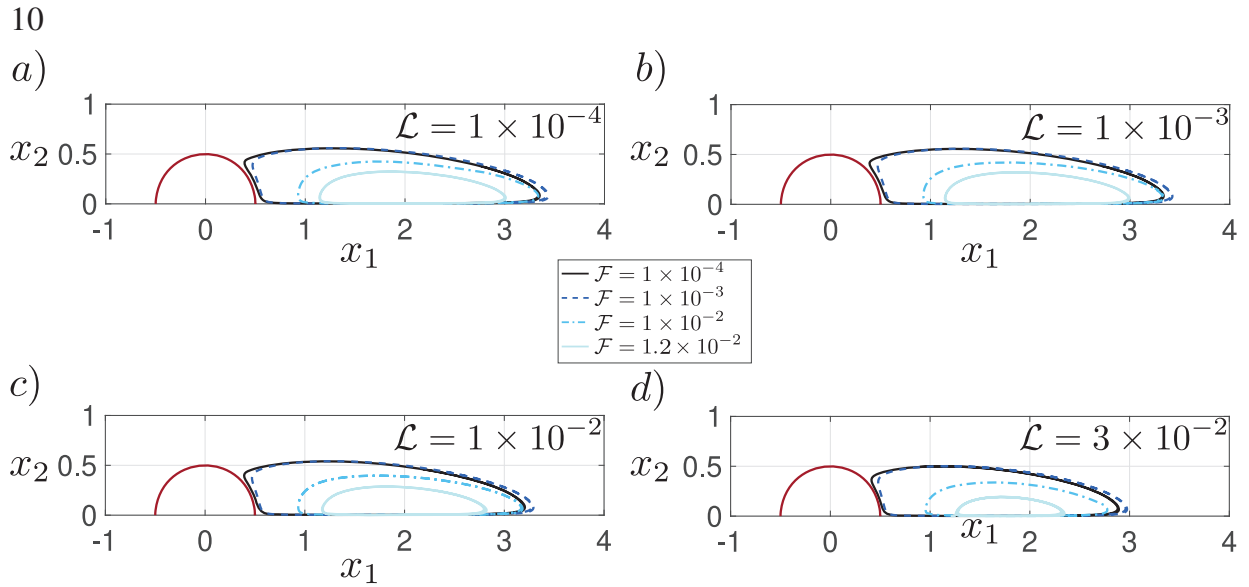


Figure 5: Streamlines identifying the recirculation region past the cylindrical permeable shell at $Re = 50$ for different values of \mathcal{F} . Each panel corresponds to a single value of \mathcal{L} .

322 to the one described in figure 4 is observed. For a fixed filtrability number, an increase in \mathcal{L}
 323 leads to a slight decrease of L_R , while X_R does not vary noticeably.

324 A complete characterization of the flow morphology requires also the analysis of the effect
 325 of the Reynolds number. In figure 6 we show the recirculation regions for fixed filtrability
 326 number $\mathcal{F} = 10^{-2}$, for different values of \mathcal{L} and for $Re = 50, 75, 100, 110$. For $Re = 50$, the
 327 flow is characterized by a recirculation detached from the body such that $L_R \approx 2$. At $Re = 75$,
 328 the recirculation region moves downstream and L_R increases. This effect is enhanced at large
 329 values of the slip number. In the last case, $Re = 110$, the recirculation region moves further
 330 downstream and L_R decreases, and eventually disappears for large values of \mathcal{L} .

331 The evolution of L_R and X_R with \mathcal{L}, \mathcal{F} and Re is summarized in figure 7. The quantities
 332 L_R and X_R have been deduced by a Matlab script which evaluates the position of the zeros
 333 of the horizontal velocity field sampled on the line $x_2 = 0$. In analogy with the solid case,
 334 L_R increases with Re (fig. 7a)). The curves are grouped in clusters. Each cluster represents
 335 different values of Re , and each curve within the cluster a different value of \mathcal{L} . For $Re = 25$,
 336 L_R decreases with \mathcal{F} until the recirculation region disappears for $\mathcal{F} \approx 10^{-2}$. A similar trend
 337 is observed for $Re = 50$, but in this case the recirculation region disappears for larger values
 338 of \mathcal{F} . For $Re > 50$, interestingly, the recirculation region grows as the filtrability number
 339 increases. L_R reaches a maximum and decreases, until the recirculation region disappears
 340 for $\mathcal{F} \approx 1.5 \times 10^{-2}$. For all cases, an increase in \mathcal{L} leads to a slight decrease of L_R , while
 341 the trend with \mathcal{F} does not change.

342 As shown in fig. 7b), the distance between the body and the recirculation region, X_R , increases
 343 with \mathcal{F} , reaching a maximum value approximately equal to 2 for $Re = 100$, while the effect
 344 of \mathcal{L} is negligible. An increase in Re leads to an increase in the distance X_R , but the trend
 345 with \mathcal{F} remains unchanged.

346 The morphology analysis of the steady wake shows that L_R and X_R are controlled by the
 347 slip and filtrability numbers. Large values of the filtrability number \mathcal{F} strongly influence the
 348 flow, implying detached and small recirculation regions, or even the absence of recirculation.
 349 The slip number \mathcal{L} slightly modifies the shape and distance of the recirculation region, for
 350 fixed filtrability number, whilst the qualitative behavior remains unchanged. An increase in
 351 the Reynolds number, for large values of \mathcal{F} , leads to an initial increase in L_R , followed by
 352 a decrease and eventually vanishing, while X_R monotonically increases. The outlined wake

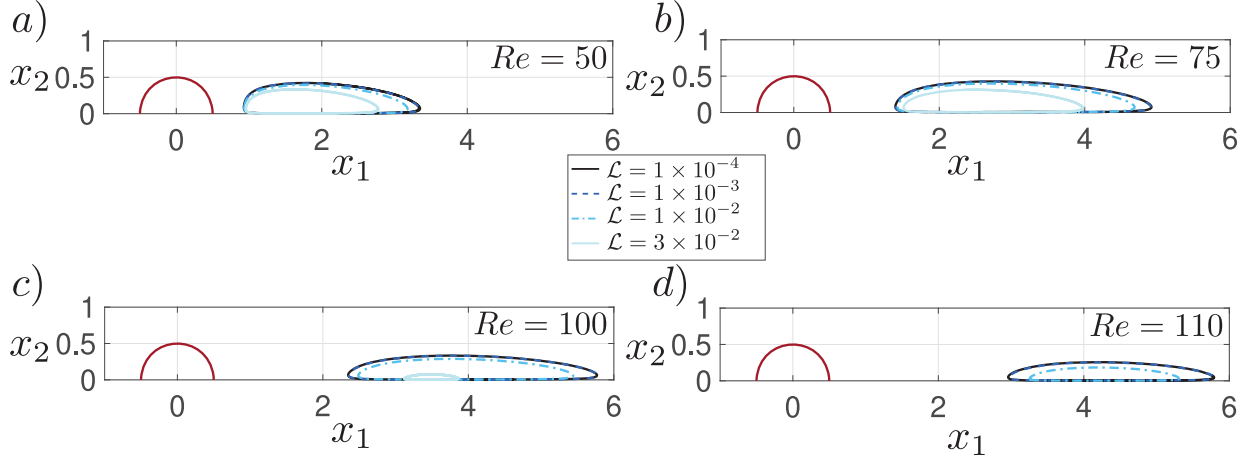


Figure 6: Streamlines identifying the recirculation region past the cylindrical permeable shell at $\mathcal{F} = 10^{-2}$ and for different values of Re and \mathcal{L} . Note that for $\mathcal{L} = 3 \times 10^{-2}$ and $Re = 110$ recirculation is suppressed.

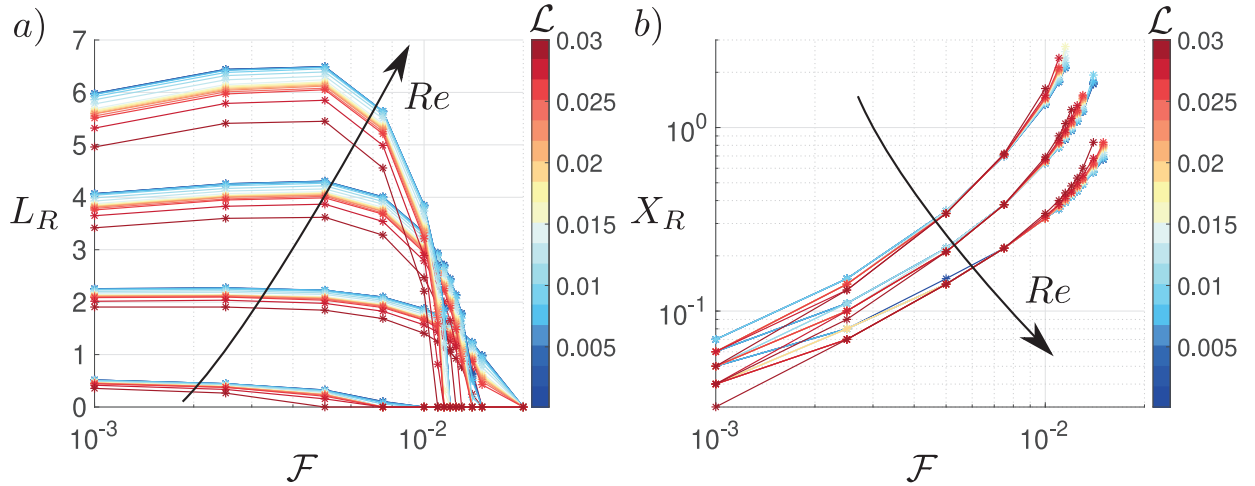


Figure 7: Panel *a*): length of the recirculation region past the cylindrical permeable shell L_R for $\mathcal{F} \in [10^{-3}, 2 \times 10^{-2}]$ and $\mathcal{L} \in [10^{-3}, 2 \times 10^{-2}]$. Each cluster represents a single value of Re . From the top to the bottom: $Re = 100, 75, 50, 25$. Panel *b*): distance of the recirculation region from the rear of the body X_R for the same values of the parameters. From the top to the bottom $Re = 50, 75, 100$.

353 morphology strongly resembles the one observed for the wake of porous rectangles (Ledda
354 *et al.* 2018), where the permeability plays a role similar to the filtrability number.

355 When the Reynolds number increases, the inertia of the fluid increases and tends to enlarge
356 the recirculation region, whereas the flow can pass through the body more easily, since the
357 velocity at the membrane is proportional to Re (equation 2.7). The result of this competition
358 is the non-monotonic behavior of the recirculation region size with Re .

359 We conclude our characterization of the steady wake past a permeable cylindrical shell by
360 considering the drag coefficient

$$361 \quad C_D = 2 \oint_{\Gamma_{\text{cyl}}} (\Sigma_{jk} (P^-, U^-) - \Sigma_{jk} (P^+, U^+)) n_k \delta_{1j} d\Gamma, \quad (3.1)$$

362 i.e. the drag exerted by the fluid over the outer ($-$) and inner ($+$) sides of Γ_{int} , respectively. The
363 drag coefficient of a solid cylinder decreases with Re (Fornberg 1980). The same behavior
364 is observed in the permeable case (cf. figure 8), where, at each value of Re , we observe
365 clusters of curves analogous to figure 7. While \mathcal{L} produces slight variations in C_D , the trend

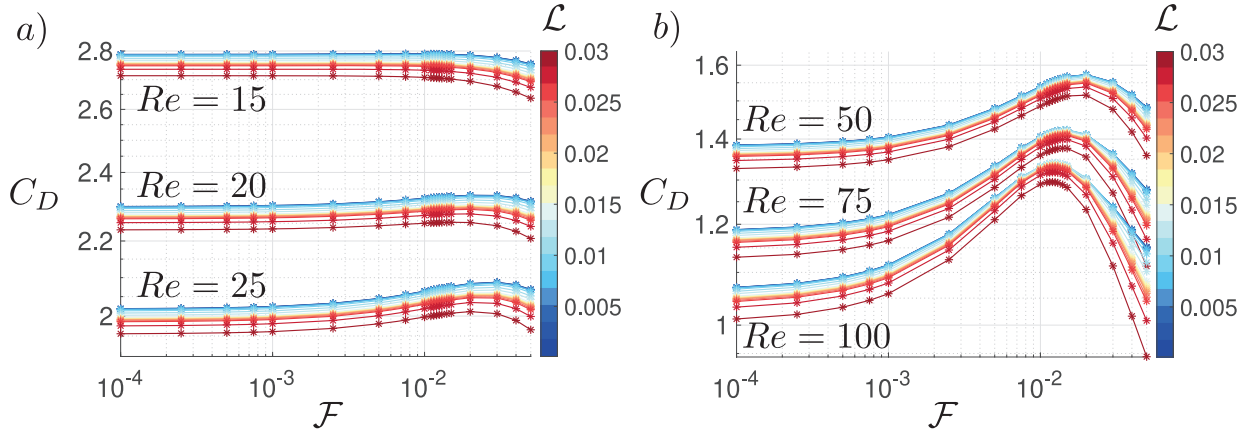


Figure 8: Variation of the drag coefficient C_D with \mathcal{F} for different values of \mathcal{L} . Each cluster in panel a) and b) corresponds to a different value of Re , as denoted in the figure.

366 in the variation with \mathcal{F} depends on the Reynolds number considered and shows two different
 367 types of behavior. Up to $Re = 15$, the drag coefficient decreases with \mathcal{F} . From $Re = 20$,
 368 C_D slightly increases with \mathcal{F} , and this effect is more pronounced as Re further increases.
 369 For larger values of Re the curve representing the C_D against \mathcal{F} is no more monotonic and
 370 for $Re = 100$, a clear peak is observed, for $\mathcal{F} \approx 1.25 \times 10^{-2}$. Surprisingly, the maximum
 371 drag coefficient $C_D \approx 1.34$ is larger than the one for the solid cylinder, $C_D \approx 1.06$ (Fornberg
 372 1980). Beyond this value of \mathcal{F} , the drag coefficient decreases.

373 In the following, a physical insight on the described drag behaviour is provided. Since the
 374 maximum is observed by varying the filtrability, while the slip does not have any significant
 375 effect on this behavior, we fix $\mathcal{L} = 10^{-4}$ and we focus on the effect of the sole \mathcal{F} in the
 376 range $[10^{-4}, 5 \times 10^{-2}]$, for $Re = 100$. Note that the maximum of the drag coefficient in
 377 this specific case is obtained for $\mathcal{F} \approx 1.2 \times 10^{-2}$, which is inside the range considered
 378 here. We perform an analysis of the different sources of drag, dividing them in a pressure
 379 contribution, i.e. $(\Delta P)n_1 = -(P^- - P^+)n_1$, and in a viscous stress contribution $(\Delta \Sigma_{1j}^v)n_j =$
 380 $(\Sigma_{1j}^v(U^-) - \Sigma_{1j}^v(U^+))n_j$, where $\Sigma_{jk}^v(U) = \frac{1}{Re}(\partial_j U_k + \partial_k U_j)$. These contributions are reported
 381 in figure 9a. The global pressure and viscous contributions to the drag are the integrals of
 382 the corresponding curves in figure 9a. Analyzing the integral of the pressure and viscous
 383 contributions we observe that (i) the viscous contribution is approximately ten times smaller
 384 than the pressure one (except for the case $\mathcal{F} = 5 \times 10^{-2}$) and (ii) the viscous contribution
 385 increases with \mathcal{F} , while the pressure contribution has a maximum at $5 \times 10^{-3} < \mathcal{F} < 10^{-2}$. As
 386 a result, the non-monotonous behavior of C_D vs \mathcal{F} can be largely explained by investigating
 387 the sole pressure contribution. In the almost-solid case, $\mathcal{F} = 10^{-4}$ (blue line), there is no
 388 fluid motion inside the cylinder, and the inner pressure is constant, as shown in the left
 389 frame of figure 9b. Therefore, the inner pressure does not contribute to the drag and the
 390 distribution of external pressure is the only responsible for integral forces. Focusing on the
 391 upper half of the cylinder ($x_2 > 0$), in the front part, for $(3/4)\pi < \alpha < \pi$, the pressure
 392 contribution is positive and becomes negative for $\pi/2 < \alpha < (3/4)\pi$. This suction region
 393 reduces the total drag since it acts on the front part of the cylinder. In the rear of the cylinder,
 394 the pressure contribution is positive with an almost constant negative value, which is the so-
 395 called base region. As the filtrability increases, a fluid motion manifests in the inner region of
 396 the cylinder, which is associated to a non-uniform distribution of inner pressure (see central
 397 frame in figure 9b). The pressure difference in the upstream part of the cylinder decreases as
 398 the filtrability increases since the membrane is progressively more permeable. Thus, an inner
 399 flow, oriented towards the downstream face of the cylinder, is generated. As a result of the

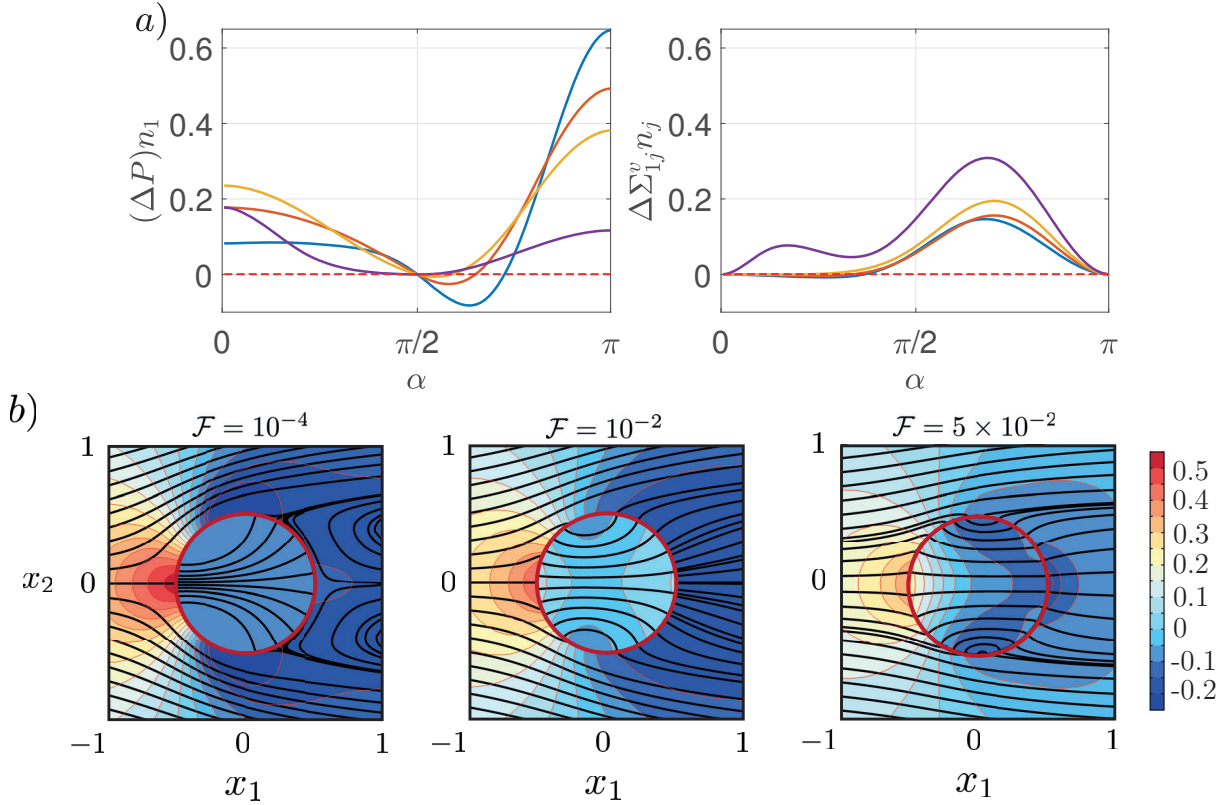


Figure 9: Panel *a*): pressure (left frame) and viscous stress (right frame) contributions to the drag following the cylinder surface. The angle α is measured counter-clockwise starting from the rear. The colours denote different values of $\mathcal{F} = 10^{-4}$ (blue), $\mathcal{F} = 5 \times 10^{-3}$ (orange), $\mathcal{F} = 10^{-2}$ (yellow), $\mathcal{F} = 5 \times 10^{-2}$ (purple). The slip number is kept fixed to $\mathcal{L} = 10^{-4}$. Panel *b*): streamlines (black bold lines) and iso-contours of the pressure for the steady flow around and through the permeable circular membrane, for different values of \mathcal{F} and $\mathcal{L} = 10^{-4}$.

400 blockage represented by the downstream cylinder face for the inner flow, the inner pressure
 401 increases moving downstream, as indicated by the concavity of the streamlines (see figures
 402 9*b*). At the same time, the external base pressure in the downstream surface of the cylinder
 403 is not significantly affected by \mathcal{F} provided that $\mathcal{F} < 10^{-2}$. As a result, the contribution to
 404 drag of the pressure difference in the downstream face of the cylinder is larger than for the
 405 solid case for $\mathcal{F} < 10^{-2}$. Figure 9*a* supports this discussion from a quantitative viewpoint.
 406 In particular, comparing cases with $\mathcal{F} < 10^{-2}$ it is possible to see that, as \mathcal{F} increases, (i)
 407 the suction at $\alpha \simeq (3/4)\pi$ decreases (thus increasing the drag), (ii) the drag contribution of
 408 the upstream face decreases and (iii) the drag contribution of the downstream face increases.
 409 At low filtrabilities, (i) and (iii) dominate over (ii), while at larger values of \mathcal{F} the term (ii)
 410 becomes predominant. Concerning the viscous contribution, although more modest, figure
 411 9*a* shows that it monotonously increases with \mathcal{F} .

412 Conversely, as \mathcal{F} is further increased, see the case $\mathcal{F} = 5 \times 10^{-2}$, the upstream contribution
 413 drastically decreases due to the larger filtrability of the membrane. The substantially higher
 414 velocities of the inner flow and the larger filtrability cause a very mild increase of the inner
 415 pressure when approaching the downstream part of the membrane. This is again shown
 416 also by the streamlines (see right frame in figure 9*b*) which are almost straight in the inner
 417 region. Moreover, the larger flow across the downstream part of the membrane decreases
 418 the pressure jump between external and internal flows in that area. As a net result, the
 419 pressure contribution to drag, in comparison with the impermeable case (here approximated
 420 by $\mathcal{F} = 10^{-4}$) decreases also in the downstream region. Although the viscous contribution

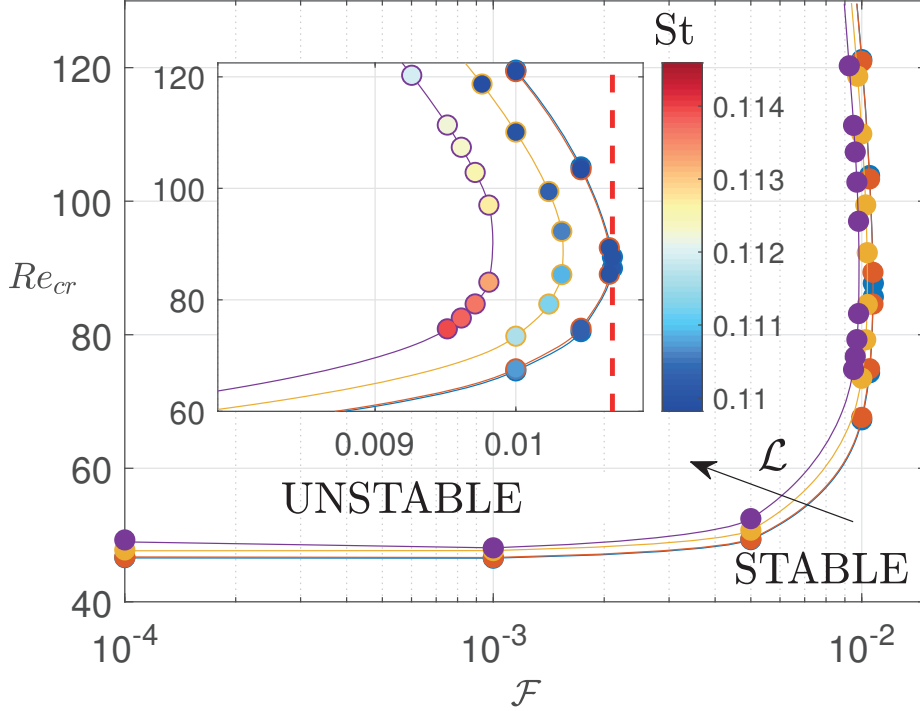


Figure 10: Marginal stability curves in the plane (\mathcal{F}, Re) . Each curve is associated with a different value of slip number $\mathcal{L} = 10^{-4}$ (blue), $\mathcal{L} = 10^{-3}$ (orange), $\mathcal{L} = 10^{-2}$ (yellow), $\mathcal{L} = 2 \times 10^{-2}$ (purple). The inset shows a zoom in for large values of \mathcal{F} . The colored bullets represent the value of the Strouhal number along the marginal stability curve in the region depicted in the inset.

421 to the drag increases, the total drag decreases because it is quantitatively dominated by the
 422 pressure, whose contribution rapidly decays.

423 In this section, we characterized the morphology of the steady flow, describing the effect
 424 of the slip and filtrability numbers. However, not all steady solutions previously described
 425 can be observed, as some of them may be unstable with respect to perturbations, thus leading
 426 to unsteady configurations. Since time-dependent simulations for every studied case (far
 427 beyond 1000) are a monumental task, we perform a stability analysis, well-known to give
 428 very accurate predictions of the bifurcations for the case at issue in computational times
 429 comparable to the ones of the steady analyses (Chomaz 2005; Theofilis 2011). Thus, in the
 430 following we study the stability of the steady flow solution as \mathcal{L} and \mathcal{F} are varied.

431 3.2. Stability analysis of the steady flow

432 As mentioned in the previous section, to complete the analysis of the chosen flow configura-
 433 tion, we now establish for which combinations of $(Re, \mathcal{F}, \mathcal{L})$ the solution is linearly stable
 434 with respect to perturbations and thus likely to be observed. The occurrence of bifurcations
 435 of the flow leading to different configurations is studied in the framework of linear stability
 436 analysis (Chomaz 2005; Theofilis 2011). We consider the flow solution as the superposition
 437 of the steady solution denoted as $[U(x, y), P(x, y)]$, outlined in the previous section, and of
 438 an infinitesimal unsteady perturbation. We thus introduce the following normal mode ansatz

$$439 \quad u_i(x, y, t) = U_i(x, y) + \sigma \hat{u}_i(x, y) \exp(\lambda t), \quad p(x, y, t) = P(x, y) + \sigma \hat{p}(x, y) \exp(\lambda t), \quad (3.2)$$

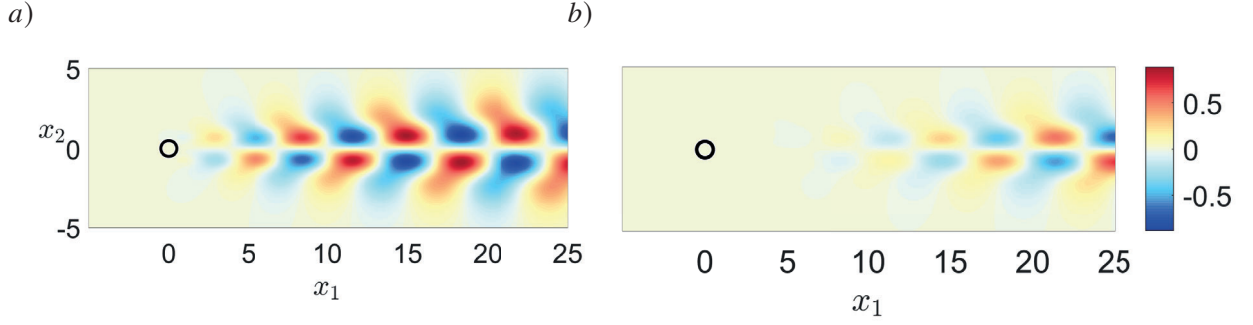


Figure 11: Real part of the eigenvector \hat{u}_1 associated with the marginally stable eigenvalue for $Re = 46.7$, $\mathcal{L} = 10^{-2}$ and $\mathcal{F} = 10^{-3}$ (panel *a*) and for $Re = 87$, $\mathcal{L} = 10^{-4}$ and $\mathcal{F} = 1.075 \times 10^{-2}$ (panel *b*). The velocity eigenvectors are normalized by their L_2 norm.

440 where $\sigma \ll 1$. At $O(1)$ the steady version of the flow equations are obtained, satisfied by
 441 $[\mathbf{U}, P]$, and at $O(\sigma)$ the following system of equations is obtained

$$442 \quad \lambda \hat{u}_i + \hat{u}_j \partial_j U_i + U_j \partial_j \hat{u}_i = -\partial_i \hat{p} + \frac{1}{Re} \partial_{jj}^2 \hat{u}_i, \quad (3.3)$$

$$443 \quad \partial_i \hat{u}_i = 0$$

$$444 \quad \hat{u}_i = \hat{u}_i^+ = \hat{u}_i^-$$

$$445 \quad \hat{u}_i = Re \mathcal{M}_{ij} (\Sigma_{jk} (\hat{\mathbf{u}}^-, \hat{p}^-) - \Sigma_{jk} (\hat{\mathbf{u}}^+, \hat{p}^+)) n_k, \quad (3.4)$$

445 together with the homogeneous Dirichlet boundary condition at the inlet Γ_{in} , $\hat{u}_1 = \hat{u}_2 = 0$,
 446 and the stress-free condition on the sides Γ_{lat} and at the outlet Γ_{out} , $(-\hat{p} \delta_{ij} + \frac{1}{Re} \partial_j \hat{u}_i) n_j = 0$.
 447 Equations (3.3, 3.4), together with the boundary conditions on Γ_{in} , Γ_{lat} , Γ_{out} , define an
 448 eigenfunction problem with, possibly, complex eigenvalues $\lambda = \text{Re}(\lambda) + i \text{Im}(\lambda)$. The real
 449 part of the eigenvalue is the growth rate of the global mode, and the imaginary part its
 450 angular velocity. We introduce the associated Strouhal number defined as $St = \frac{\text{Im}(\lambda)}{2\pi}$. The
 451 flow is asymptotically unstable if there exists at least one eigenvalue with positive real part,
 452 otherwise it is asymptotically stable. The absence of unstable modes therefore ensures the
 453 occurrence of the steady solution, while their presence gives useful information about the
 454 emerging unsteady flow configuration.

455 We turn now to describe the results of the linear stability analysis. The solid case exhibits
 456 a Hopf bifurcation at $Re = 46.7$ that drives the flow to a state that is periodic in time,
 457 characterized by the alternate shedding of vortices, the so-called von Kármán vortex street
 458 (Barkley 2006). Ledda *et al.* (2018) showed the suppression of this vortex shedding mode
 459 for large enough values of the permeability, in the case of porous rectangular cylinders. A
 460 preliminary analysis on the permeable membrane shows that the above-described mode is
 461 also the only one that destabilizes the steady wake in the range $10 < Re < 130$. In figure
 462 10 we report the marginal stability curves (i.e. the locus of points with $\text{Re}(\lambda) = 0$) in the
 463 (\mathcal{F}, Re) plane, for different values of \mathcal{L} . The marginal stability curves define a stable and an
 464 unstable region in the (\mathcal{F}, Re) plane. At low values of \mathcal{F} and \mathcal{L} , the critical Reynolds number
 465 Re_{cr} for the marginal stability coincides with the solid one, i.e. $Re_{cr} = 46.7$. An increase
 466 in \mathcal{L} leads to a slight increase in Re_{cr} that reaches a maximum approximately equal to 50
 467 for $\mathcal{L} = 0.02$. For $\mathcal{F} > 10^{-3}$ the critical Reynolds number increases. We identify a critical
 468 value of $\mathcal{F} = \mathcal{F}_{cr}$ beyond which the steady solution is stable. This value depends on the
 469 Reynolds and slip numbers. For fixed \mathcal{L} , \mathcal{F}_{cr} initially increases with Re , reaches a maximum
 470 and decreases. Among all cases, the maximum value $\mathcal{F}_{cr} \approx 1.08 \times 10^{-2}$ is achieved for
 471 $\mathcal{L} \approx 10^{-4}$.

472 The imaginary part of the eigenvalue well approximates the oscillation frequency of the

473 nonlinear limit cycle in marginal stability conditions (Barkley 2006). In the inset of figure
 474 10, we report the value of the Strouhal number along the marginal stability curve. We do
 475 not observe substantial variations in the Strouhal number with respect to the solid case, i.e.
 476 $St \approx 0.116$ (Norberg 2003).

477 In figure 11 we report the spatial distribution of $Re(\hat{u}_1)$ for two different cases, on panel
 478 *a*) characterized by a recirculation region close to the cylinder, and on panel *b*) characterized
 479 by a recirculation region far downstream. In both cases, the unstable mode leads to a vortex
 480 shedding similar to the solid case one, as already anticipated. As the recirculation region
 481 moves downstream, the onset of the vortex shedding is displaced downstream and the flow
 482 in proximity of the cylinder is almost steady.

483 The analysis of the stability properties of the steady wake shows the strong stabilization
 484 effect of the filtrability number. The marginal stability curves strongly resemble those outlined
 485 in Ledda *et al.* (2018, 2019). In particular, the vortex shedding is suppressed for large enough
 486 values of the filtrability. This similarity is confirmed by the spatial distribution of the unstable
 487 mode, that moves downstream with the recirculation region of the steady flow. Indeed, the
 488 stability properties of the wake can be related to the extent of the so-called *absolute region of*
 489 *instability* in a local stability analysis (i.e. performed for the velocity profile at each streamwise
 490 location, see Monkewitz 1988; Giannetti & Luchini 2007), that roughly corresponds to the
 491 recirculation region. As shown in Ledda *et al.* (2018), there is a critical value of the extent
 492 of the recirculation region beyond which the flow becomes unstable. When large values of
 493 the filtrability are considered, the recirculation region is small or even absent, and thus the
 494 vortex shedding is suppressed. For fixed $\mathcal{F} \approx 10^{-2}$ and \mathcal{L} and increasing Re , the recirculation
 495 region initially increases and then decreases its dimensions (cf. figure 6). Therefore, the first
 496 destabilization and subsequent stabilization for fixed \mathcal{F} and \mathcal{L} is due to the non-monotonic
 497 behavior of the length of the recirculation region with Re , which crosses the critical value
 498 for the marginal stability twice.

499 By comparing the marginal stability curve with the drag coefficient, we deduce that the
 500 maximum of C_D for the steady flow occurs for a stable configuration for all values of Re .
 501 Interestingly, a permeable circular membrane exhibits a larger drag than the equivalent solid
 502 one, and this maximum occurs when the steady flow is stable.

503 In the present section, we performed a parametric study under the framework of bifurcation
 504 theory in order to exclude the unstable configurations from the variety of steady solutions
 505 obtained in Section 3.1. In the next section, we propose a methodology to obtain the full-
 506 scale design of the structure by fulfilling some objectives on the macroscopic behavior of the
 507 steady flow, under the constraint of stable configuration.

508 4. From objectives to full-scale design

509 In the previous section, we performed a parametric study on the steady solution of equations
 510 (2.6, 2.7) and the stability properties of the resulting wake, considering \mathcal{L} and \mathcal{F} as free
 511 parameters. In the present section, we outline a procedure for the objective-based full-scale
 512 design of the permeable circular membrane. We first define macroscopic objectives to be
 513 fulfilled and, performing microscopic simulations, we identify the geometry which best
 514 satisfies the macroscopic requirements. We consider cylindrical permeable shells formed by
 515 an array of elliptical inclusions, distributed with a constant angular distance, of axes l_t and
 516 l_n (normalized with the microscopic characteristic length) aligned along the tangential and
 517 normal directions to the membrane, respectively, in the range $0.02 < l_t, l_n < 0.98$.

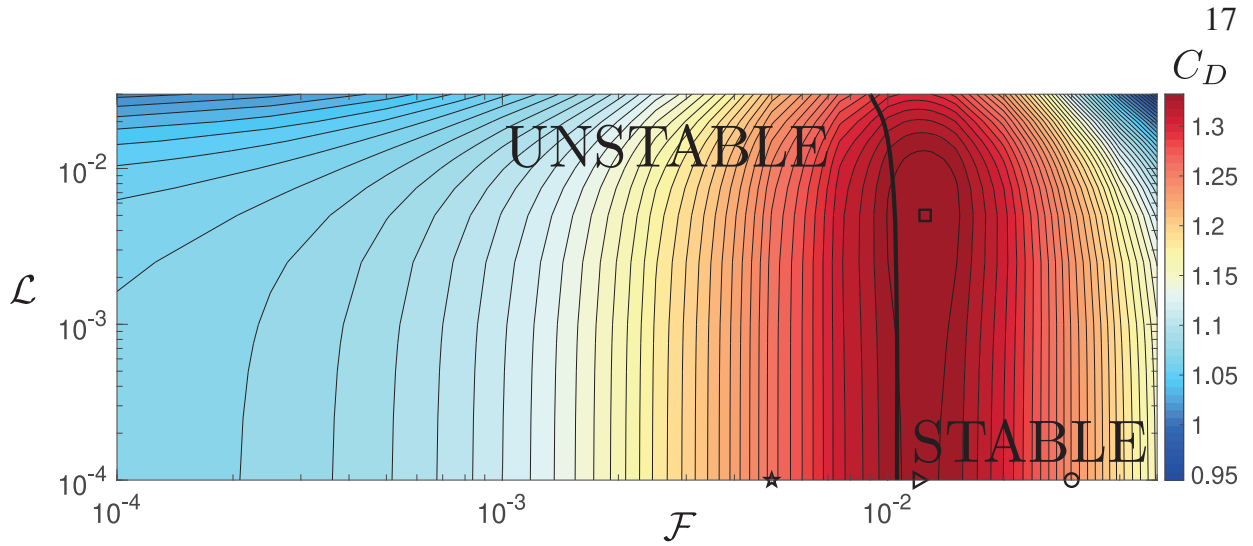


Figure 12: Isocontours of C_D for $Re = 100$ in the $(\mathcal{F}, \mathcal{L})$ plane. Symbols identify the configurations listed in table 1. The marginal stability curve for the value of Re considered is represented by a bold solid line (all cases on the right side of the curve are stable).

518

4.1. Choosing the design objective

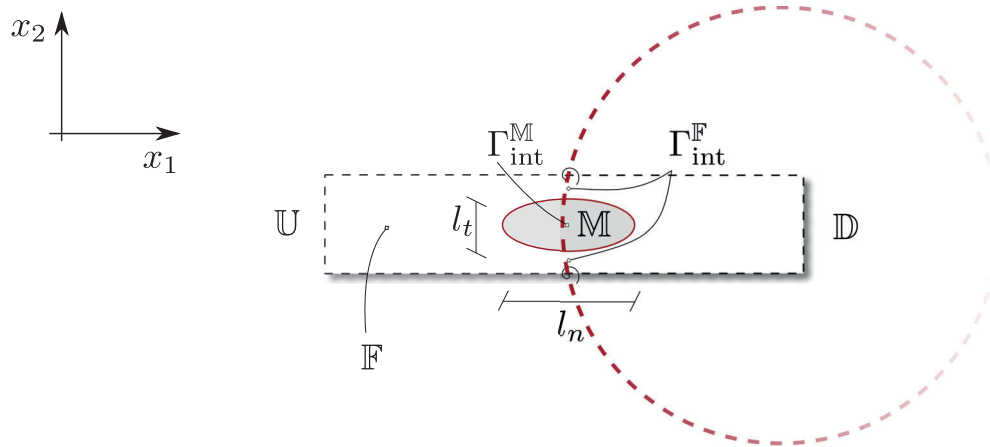
519 An important macroscopic property is the drag exerted on the solid structure by the incoming
 520 fluid. Several attempts of controlling this integral quantity, defined by equation (3.1), by
 521 permeable surfaces have been carried out, some of them focused on minimizing the drag
 522 (Garcia-Mayoral & Jiménez 2011; Abderrahaman-Elena & García-Mayoral 2017; Gómez-de
 523 Segura & García-Mayoral 2019), others investigating the conditions for drag maximization
 524 (Cummins *et al.* 2017, 2018).

525 We fix $Re = 100$ and we study the variation of C_D with \mathcal{L} and \mathcal{F} . In figure 12 we
 526 report the iso-contours of C_D on the $(\mathcal{F}, \mathcal{L})$ plane. The bold solid line corresponds to the
 527 marginal stability boundary for $Re = 100$. Among all these possible solutions for the drag
 528 coefficient, we select the maximum value of the drag coefficient ($C_D = 1.339$), which occurs
 529 at $\mathcal{F} = 1.25 \times 10^{-2}$, $\mathcal{L} = 5 \times 10^{-3}$ (denoted by \square in figure 12) and in the following will be
 530 compared with the full-scale simulations. For the sake of completeness, we select other three
 531 values of C_D denoted by $\circ, \triangleright, \star$ in figure 12, to verify the faithfulness of the homogenized
 532 model in the parameters space $(\mathcal{F}, \mathcal{L})$ for constant $\mathcal{L} = 10^{-4}$. Note that the case denoted
 533 with \star is unstable, but we use it as an additional test case owing to the large recirculation
 534 region that this configuration exhibits.

535 4.2. Linking the microscopic geometry to the macroscopic properties: elliptical inclusions

536 We now turn to describe the procedure for the determination of the microscopic geometry
 537 based on the macroscopic flow properties identified in the previous subsection. We first
 538 perform microscopic simulations in the domain depicted in figure 13a (dashed rectangle)
 539 whose lengths are adimensionalized with the microscopic length ℓ , so that the results do not
 540 depend on the separation of scales parameter $\varepsilon = \frac{\ell}{D}$, according to Zampogna & Gallaire
 541 (2020). Within this domain, two different microscopic problems need to be solved to calculate

a)



b)

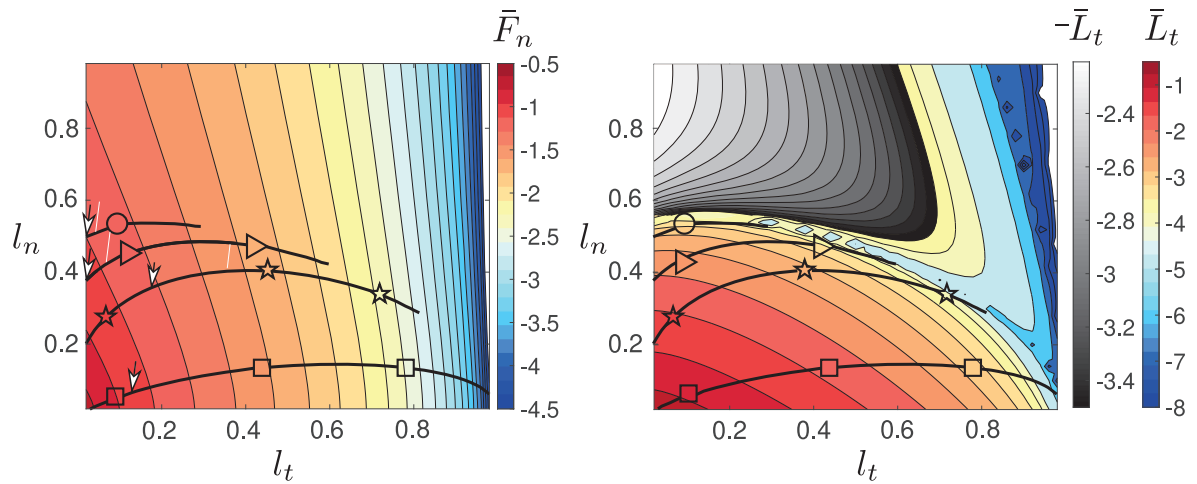


Figure 13: Panel a): Sketch of the membrane (red dashed line) with a zoom on the microscopic elementary cell used to calculate \bar{L}_t and \bar{F}_n . The tangential- and normal-to-the-interface axes of the solid inclusion are respectively denoted with l_t and l_n and normalized by ℓ . Panel b): isocontours of $\bar{F}_n = \frac{\mathcal{F}}{\varepsilon}$ (left) and $\bar{L}_t = \frac{\mathcal{L}}{\varepsilon}$ (right) on the plane (l_t, l_n) , in logarithmic scale. Blue-to-red colors indicate positive values of \bar{F}_n and \bar{L}_t while gray-scale refers to negative values of \bar{L}_t . The lines identify the isocontours of the possible couples (l_n, l_t) whose symbols correspond to different couples $(\mathcal{F}, \mathcal{L})$ of figure 12. Each point on those lines is a good candidate to realize the desired value of \mathcal{F} and \mathcal{L} , upon adjustment of the value of ε . The selected values of l_t and l_n are labelled with white arrows for each case.

542 \bar{F}_n and \bar{L}_t ; they read respectively

$$\begin{aligned}
 -\partial_i Q + \partial_{tt}^2 F_i &= 0 && \text{in } \mathbb{F} \\
 \partial_i F_i &= 0 && \text{in } \mathbb{F} \\
 F_i &= 0 && \text{on } \partial\mathbb{M} \\
 \Sigma_{nn}(Q, \mathbf{F}) &= -1 && \text{on } \mathbb{U} \\
 \Sigma_{nn}(Q, \mathbf{F}) &= 0 && \text{on } \mathbb{D} \\
 F_i, Q &&& \text{periodic along } \mathbf{t}
 \end{aligned} \tag{4.1}$$

543

544 and

$$\begin{aligned}
 -\partial_i R + \partial_{ll}^2 L_i &= 0 && \text{in } \mathbb{F} \\
 \partial_i L_i &= 0 && \text{in } \mathbb{F} \\
 L_i &= 0 && \text{on } \partial\mathbb{M} \\
 \Sigma_{tn}(R, \mathbf{L}) &= -1 && \text{on } \mathbb{U} \\
 \Sigma_{tn}(R, \mathbf{L}) &= 0 && \text{on } \mathbb{D} \\
 L_i, R &&& \text{periodic along } \mathbf{t},
 \end{aligned} \tag{4.2}$$

546 where $i, l = t, n$, i.e. the equations are written in the local frame of reference of the cylinder
 547 surface. We refer to figure 13a for a definition of \mathbb{F} , \mathbb{M} , \mathbb{U} and \mathbb{D} . In the microscopic problems
 548 (4.1) and (4.2) the scalar fields R and Q appear. They relate the value of the pressure on
 549 Γ_{int} to the upward and downward fluid stresses and do not contribute to the determination of
 550 the macroscopic flow through the membrane (cf. Zampogna & Gallaire (2020) for a detailed
 551 explanation). In the purpose of the present work, we are not directly interested in microscopic
 552 fields representing the solution of these problems, but we need only to know the quantities
 553 \bar{F}_n and \bar{L}_t which appear in the macroscopic model via equation (2.9), where the symbol $\bar{\cdot}$
 554 denotes the spatial average used in Zampogna & Gallaire (2020), i.e.

$$\bar{\cdot} = \lim_{\mathbb{U} \rightarrow \mathbb{D}} \frac{1}{|\mathbb{F} \cup \mathbb{M}|} \int_{\mathbb{F}} \cdot \, d\mathbf{x} = \frac{1}{|\Gamma_{\text{int}}^{\mathbb{F}} \cup \Gamma_{\text{int}}^{\mathbb{M}}|} \int_{\Gamma_{\text{int}}^{\mathbb{F}}} \cdot \, d\mathbf{x}, \tag{4.3}$$

556 with $\Gamma_{\text{int}}^{\mathbb{F}}$ and $\Gamma_{\text{int}}^{\mathbb{M}}$ the fluid and solid parts of Γ_{int} within the unit cell, as sketched in figure
 557 13a. The linear problems (4.1) and (4.2) are numerically solved for each couple (l_t, l_n) ,
 558 $0.02 < l_t, l_n < 0.98$ (with a step of 0.01), via their weak formulation implemented in
 559 the finite-element solver COMSOL Multiphysics. The spatial discretization is based on
 560 the Taylor–Hood (P2-P1) triangular elements for \mathbf{F} - \mathbf{L} and R - Q , respectively. We refer to
 561 Zampogna & Gallaire (2020) for further detail about the solution of the microscopic problems.

562 After averaging the solution of the microscopic problems, we deduce \bar{F}_n and \bar{L}_t , whose
 563 isocontours are reported in figure 13b as functions of the two axes l_n and l_t .

564 The parameters \mathcal{F} and \mathcal{L} are then calculated by a renormalization of \bar{F}_n and \bar{L}_t with
 565 respect to the macroscopic length scale, i.e.

$$\mathcal{F} = \varepsilon \bar{F}_n \quad \text{and} \quad \mathcal{L} = \varepsilon \bar{L}_t. \tag{4.4}$$

567 While in a direct approach the parameters defining the full scale geometry l_t , l_n and ε
 568 are given and the corresponding filtrability and slip numbers are evaluated, in the inverse
 569 procedure they need to be determined based on the choice of a given property that has to be
 570 satisfied by the fluid flow. Actually, there is no one-to-one relation linking \mathcal{F} and \mathcal{L} to the
 571 microscopic geometry. Once filtrability and slip are chosen, one has potentially full freedom
 572 in the choice of the microscopic structure. This choice is essentially related to the geometrical
 573 shape of the microscopic inclusions, in this case ellipsoidal ones with variable axes, and to
 574 their relative size with respect to the macroscopic length, as outlined in figure 13b, where
 575 several configurations satisfy the desired values of \mathcal{F} and \mathcal{L} , each one associated with a value
 576 of ε . For the sake of clarity we list the steps to follow in order to determine these geometrical
 577 parameters which allow us to define the microscopic geometry of the permeable shell:

- 578 • According to the previous subsection, we identify a pair $(\mathcal{F}, \mathcal{L}) = (\mathcal{F}^*, \mathcal{L}^*)$ of interest.
- 579 • We find in the $l_t - l_n$ plane the possible pairs of (l_t, l_n) that can give the correct set
 580 $(\mathcal{F}^*, \mathcal{L}^*)$. These values are found by evaluating the ratio $\mathcal{F}^*/\mathcal{L}^*$, which is not depending
 581 on ε (since F_n and L_t are proportional to ε). The potential values of l_n and l_t are those
 582 associated to the black solid lines in figure 13b, which realize C_D^* upon renormalization by
 583 the proper value of ε that is still undetermined.

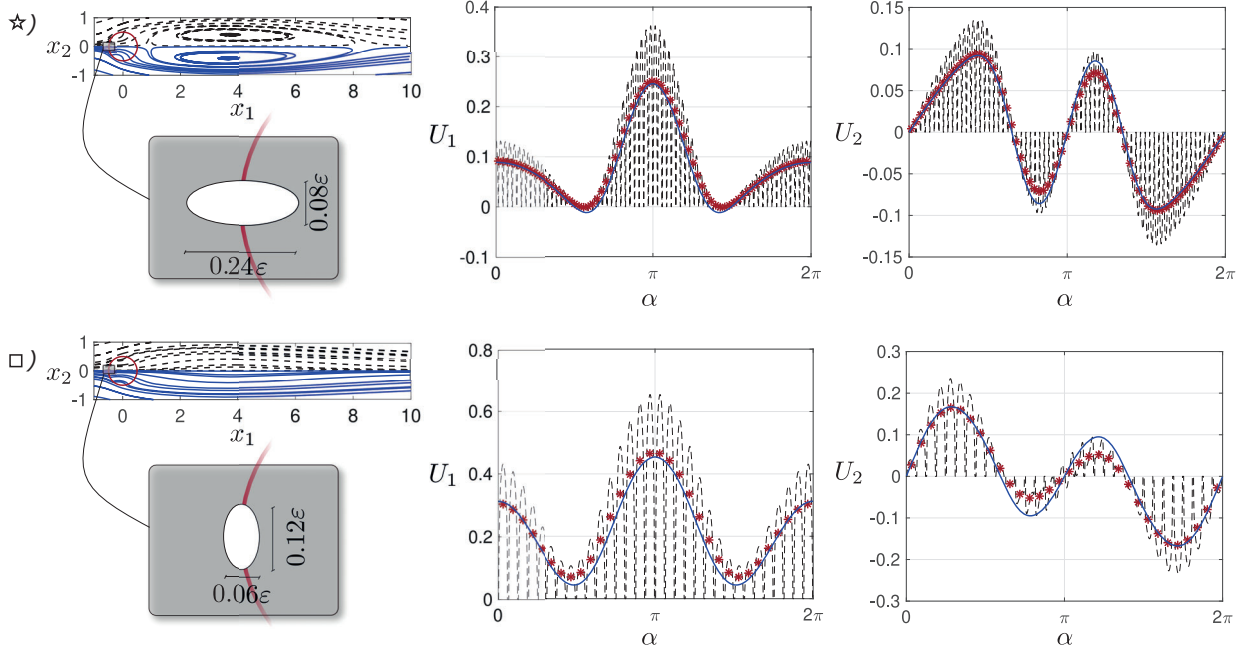


Figure 14: Comparison between full-scale and equivalent model for case \star and \square identified in figure 12. The microscopic geometry forming the cylindrical shell, sketched for each case in the grey insets on the left, is the result of the inverse procedure explained in Section 4.2. Left column: flow streamlines for the full scale case (black dashed lines) and for the macroscopic model (blue solid lines). Central and right column: horizontal and vertical velocities, U_1 and U_2 sampled on the cylindrical shell using the angle α measured counterclockwise starting from the rear. Dashed lines represent the full-scale model, blue lines the macroscopic model and red stars the average of the full-scale model, calculated applying a discrete version of the integral in equation (4.3), based on a 1-point Gaussian rule, to the velocity profile in each microscopic elementary cell forming the membrane. Numerical values of ϵ , \mathcal{F} , \mathcal{L} and other representative values of the fluid flow (C_D , X_R , L_R) are listed in table 1 for each case.

584 • Among the potential candidates, the final value of ϵ and thus the values of (l_t, l_n) can
 585 be chosen based on other constraints (like, for instance, the minimization of microscopic
 586 anisotropy, i.e. $l_t \approx l_n$, the minimization of ϵ or the satisfaction of geometrical properties of
 587 the medium like the fluid-to-solid ratio).

588 • Once the value of ϵ is selected, there is only one couple (l_t, l_n) that satisfies the
 589 macroscopic values of $\mathcal{F}^* = \epsilon \bar{F}_n$ and $\mathcal{L}^* = \epsilon \bar{L}_t$. We then deduce \bar{F}_n and \bar{L}_t , and eventually
 590 l_t and l_n .

591 The values of ϵ , l_t and l_n are deduced for each case highlighted by the symbols in figure 12.
 592 Table 1 shows the values found for each case, corresponding to the white pointers in figure
 593 13b. For the cases denoted by \circ , \triangleright and \square the values of (l_t, l_n) have been chosen so as to
 594 obtain a value of ϵ of order 10^{-1} , while for the case \star the value of (l_t, l_n) guarantees minimal
 595 anisotropy with the constraint $\epsilon \leq 0.045$.

596 The final full-scale geometries are thus obtained by distributing the inclusions along the
 597 membrane centerline Γ_{int} , with a constant angular distance among them given by $\Delta\phi =$
 598 $2\pi \lfloor \frac{\epsilon}{\pi} \rfloor$, with $\lfloor \cdot \rfloor$ the integer part in order to have an integer number of inclusions along the
 599 cylindrical shell. Two examples of microscopic geometries obtained are depicted in figure 14,
 600 where 69 and 32 inclusions are employed. Once the full-scale geometry is built the reliability
 601 of the inverse procedure is verified as explained in the next section.

	N	ε	l_t	l_n	\mathcal{F}	\mathcal{L}	C_D	C_D^{EQ}	L_R	L_R^{EQ}	X_R	X_R^{EQ}
★	69	4.49×10^{-2}	0.08	0.24	5.0×10^{-3}	1.0×10^{-4}	1.264	1.259	7.386	7.358	0.431	0.421
□	32	9.82×10^{-2}	0.12	0.06	1.25×10^{-2}	5.00×10^{-3}	1.338	1.339	–	–	–	–
▷	31	1.01×10^{-1}	0.02	0.38	1.2×10^{-2}	1.0×10^{-4}	1.350	1.334	–	–	–	–
○	10	3.14×10^{-1}	0.02	0.50	3.0×10^{-2}	1.0×10^{-4}	1.365	1.239	–	–	–	–

Table 1: Relevant geometrical and physical parameters for the cases chosen in figure 12; N indicates the number of inclusions forming the membrane, the superscript EQ denotes quantities calculated using model (2.7) on Γ_{int} while the absence of superscript denotes quantities evaluated from the full-scale solution.

602

4.3. Comparison between the homogenized and the full-scale results

603

604

605

606

607

608

609

610

611

612

613

614

615

616

617

618

619

620

621

622

623

624

625

626

627

628

629

630

631

632

633

634

635

636

637

638

We verify the faithfulness of the homogenization approach and the subsequent retrieval of the microscopic geometry by comparing the results obtained using the equivalent model with the feature-resolved flow past the full-scale permeable shell. To deduce the full-scale flow, the Navier-Stokes equations are solved in the full-scale domain, where each solid inclusion forming the membrane is explicitly taken into account in the fluid domain and thus in the mesh. The full-scale problem is solved by the finite-element solver COMSOL Multiphysics, using the same numerical setup as for the macroscopic flow solution. In order to have spatially converged results, mesh M1 (cf. table 2) has been modified in the vicinity of the full scale structure. A circular refinement region of diameter $1.1L$ has been added with a resolution chosen in order to guarantee at least 10^2 cells between two adjacent solid inclusions whose boundary has been discretized using at least 50 segments. The boundary conditions on Γ_{in} , Γ_{out} and Γ_{lat} are the same as in the case of the macroscopic model (2.7), while we impose a no-slip condition on the walls of each microscopic inclusion, i.e. $u_i|_{\Gamma_{\partial M}} = 0$.

In figure 14 we report two sample comparisons of the flow fields obtained with the homogenized model and with the full-scale simulations (cases ★ and □ identified in figure 12), together with the velocities at the membrane. In both cases, we observe a good agreement between the two approaches, with an error on the velocities along the membrane of the order of ε , as expected.

In table 1 we report the reference values (C_D , L_R , X_R) for all cases identified in figure 12. Also in this case, we observe an overall good agreement, even for extremely large values of ε , which are far beyond the rigorous domain of validity of the theory. Only for the case denoted by ○ the differences in the C_D are non-negligible, suggesting that a maximum value of ε beyond which macroscopic model (2.7) is no more applicable lies between 10^{-1} and 3.5×10^{-1} . A complete validation also requires the comparison of the stability properties of the flow between homogenized model and full-scale simulations, reported in figure 15. We observe a good agreement between the spectra, and in particular the leading eigenvalues are well described by the homogenized model. Considering the one with largest real part, the relative errors on the absolute value are 0.25% for the case ★ ($\lambda = 0.076 + 0.64i$), and 0.6% for the case □ ($\lambda = -0.039 + 0.72i$). We finally stress the importance of the validation described above, since it constitutes a strong proof of the faithfulness of the model developed in Zampogna & Gallaire (2020) in the case of flows with non-negligible macroscopic inertia.

In this section, we outlined a method for the geometrical reconstruction of the microscopic geometry based on the macroscopic properties of the membrane, thus concluding the first branch of the scheme described by figure 3. We note that the homogenized model, combined with the stability analysis technique, allows us to perform a parametric study spanning a massive range of possible geometries with extremely fast outputs. The flow through the

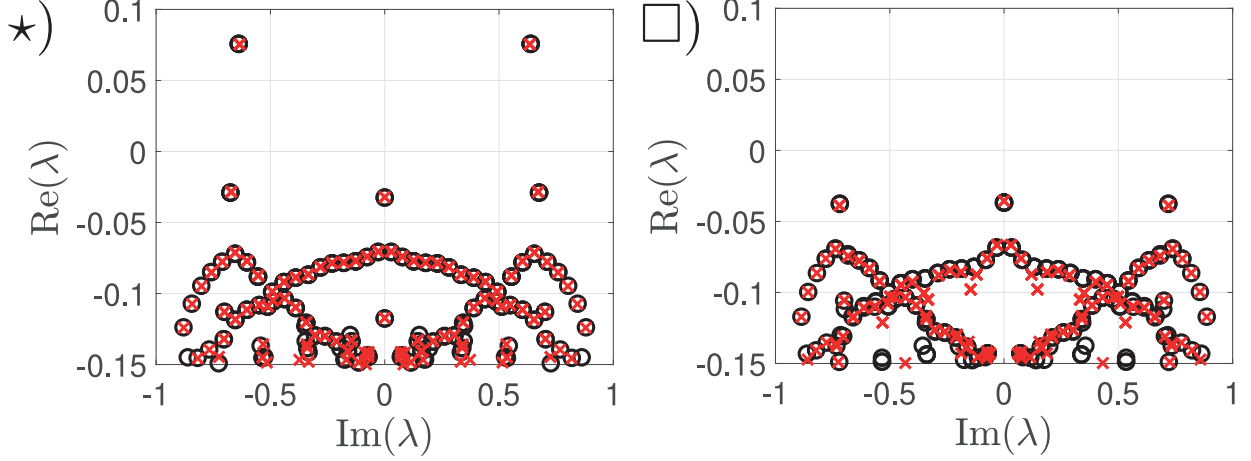


Figure 15: Comparison between the homogenized and full-scale results of the stability analysis. The crosses and the circles denote the eigenvalues obtained from the full-scale structure and from the homogenized model, respectively, for the two reported cases.

639 resulting microscopic structure shows a good agreement with the homogenized model, thus
 640 giving confidence to the parametric study carried out in Section 3. We verified the validity of
 641 the homogenized model through permeable membranes for Reynolds numbers of the order of
 642 10^2 . The error on the final solution is of order ε , thus degrading the solution when extremely
 643 large values of ε are considered. Nevertheless, the homogenized model gives also in these
 644 cases fairly reasonable results that can be used as guidelines in a first parametric study, before
 645 optimizing the resulting microscopic structure.

646 The previous analysis was focused on membranes with monodisperse and identical
 647 microscopic inclusions along the centerline of the membrane. In the following, we analyze
 648 the opportunity to exploit membranes of variable permeability by employing a Lagrangian-
 649 based optimization, i.e. we focus on the second branch of the diagram of figure 3, in the
 650 inverse procedure part.

651 5. Adjoint-based optimization of membranes of variable properties

652 The purpose of the present section consists of finding profiles of \mathcal{F} and \mathcal{L} which are *optimal*
 653 with respect to a given objective, here specifically the maximization of the drag coefficient.
 654 To accomplish this task, a variational approach is used.

655 5.1. Sensitivity with respect to variations of the slip and filtrability numbers

656 In this section, we introduce the theoretical framework for the adjoint-based optimization of
 657 the structure of the membrane. We recall that, at the interface, we denote with the superscript
 658 \cdot^+ the variables evaluated in the inner part of the cylinder and with \cdot^- those evaluated in the
 659 outer part. Any small modification $\delta\mathcal{M}_{ij}$ of the tensor component \mathcal{M}_{ij} (i.e. variations of \mathcal{F}
 660 or \mathcal{L}) induces a perturbation $(\delta\mathbf{u}, \delta p)$ on the flow field such that $(\mathbf{u}, p) = (\mathbf{U} + \delta\mathbf{u}, P + \delta p)$.
 661 The drag coefficient, i.e. the objective in the Lagrangian framework, is written as follows:

$$662 \quad C_D = 2 \oint_{\Gamma_{\text{cyl}}} (\Sigma_{jk} (p^-, \mathbf{u}^-) - \Sigma_{jk} (p^+, \mathbf{u}^+)) n_k \delta_{1j} \, d\Gamma. \quad (5.1)$$

663 The modification $\delta\mathcal{M}_{ij}$ thus perturbs the drag by δC_D according to

$$664 \quad \delta C_D = 2 \oint_{\Gamma_{\text{cyl}}} (\Sigma_{jk} (\delta p^-, \delta \mathbf{u}^-) - \Sigma_{jk} (\delta p^+, \delta \mathbf{u}^+)) n_k \delta_{1j} \, d\Gamma = \oint_{\Gamma_{\text{cyl}}} \nabla_{\mathcal{M}_{ij}} C_D \delta \mathcal{M}_{ij} \, d\Gamma, \quad (5.2)$$

665 The quantities $(\delta \mathbf{u}^\pm, \delta p^\pm)$ are the solution of equation (B 3) reported in Appendix B, where
 666 a formal derivation of the sensitivity functions (i.e. the functions describing the variations
 667 of the objective C_D with respect to the control variable \mathcal{F} and \mathcal{L}) is carried out. In the
 668 Lagrangian framework, the sensitivities of the drag coefficient with respect to variations of
 669 \mathcal{L} and \mathcal{F} are

$$670 \quad \nabla_{\mathcal{F}} C_D = -Re u_i^{\dagger\dagger} (\Sigma_{jk} (P^-, U^-) - \Sigma_{jk} (P^+, U^+)) n_i n_j n_k \quad (5.3)$$

671 and

$$672 \quad \nabla_{\mathcal{L}} C_D = Re u_i^{\dagger\dagger} (\Sigma_{jk} (P^-, U^-) - \Sigma_{jk} (P^+, U^+)) t_i t_j n_k, \quad (5.4)$$

673 where the Lagrange multipliers $(\mathbf{u}^\dagger, p^\dagger, \mathbf{u}^{\dagger\dagger})$, also called adjoint variables, are the solution
 674 of the following linear problem

$$675 \quad \begin{aligned} \partial_i u_i^\dagger &= 0, & u_j^\dagger \partial_i U_j - U_j \partial_j u_i^\dagger &= \partial_i p^\dagger + \frac{1}{Re} \partial_{jj}^2 u_i^\dagger && \text{in } \Omega \\ (\Sigma_{ik} (-p^{\dagger-}, \mathbf{u}^{\dagger-}) - \Sigma_{ik} (-p^{\dagger+}, \mathbf{u}^{\dagger+})) n_k - u_i^{\dagger\dagger} &= 0 && \text{on } \Gamma_{\text{int}} \\ u_i^{\dagger\dagger} &= u_i^{\dagger-} && \text{on } \Gamma_{\text{int}} \end{aligned} \quad (5.5)$$

676 and

$$677 \quad u_i^{\dagger\dagger} = Re^{-1} \mathcal{M}_{ji}^{-1} (u_j^{\dagger-} - 2\delta_{1j}) \quad \text{on } \Gamma_{\text{int}}, \quad (5.6)$$

678 together with the adjoint boundary conditions $u_i^\dagger = 0$ at the inflow, $\partial_2 u_1^\dagger = u_2^\dagger = 0$ at the
 679 transverse boundaries and $\Sigma_{ik} (-p^\dagger, \mathbf{u}^\dagger) n_k + u_k n_k u_i^\dagger = 0$ at the outflow. At this point, it is
 680 clear that in order to understand how the control variables \mathcal{F} and \mathcal{L} influence the objective
 681 function C_D via equations (5.3, 5.4), the linear problem (5.5) has to be solved, without
 682 the necessity to explicitly evaluate the perturbed state $(\mathbf{u}, p) = (\mathbf{U} + \delta \mathbf{u}, P + \delta p)$. The linear
 683 adjoint problem presents an advantage in terms of computational time with respect to the non-
 684 linear problem for (\mathbf{u}, p) , and is suitable for a gradient-based optimization with a progressive
 685 update of the distribution of the membrane properties.

686 In figure 16a we report the variation of the drag coefficient with \mathcal{F} , for fixed $\mathcal{L} = 5 \times 10^{-3}$
 687 (black dots), together with the prediction given by the sensitivity analysis (solid lines), close
 688 to the configuration of maximum C_D identified by the \square symbol in figure 12. Note that, at
 689 this stage, we keep \mathcal{F} uniform along the membrane. A good agreement is observed, in the
 690 vicinity of the points where the sensitivity is evaluated, i.e. $\delta \mathcal{F} \approx 0.01 \mathcal{F}$. The deviation
 691 becomes more important for variations larger than $\delta \mathcal{F} \approx 0.01 \mathcal{F}$, showing a rather strong
 692 effect of non-linearities close to the point of the maximum drag coefficient. In figure 16b we
 693 show the distribution of sensitivity along the upper part of the cylinder, for three cases. The
 694 distribution exhibits a non-monotonic behavior, with positive values in the front and in the
 695 middle of the membrane, and negative values close to the rear of the cylinder.

696 The same analysis is performed for uniform variations of \mathcal{L} (figure 17). In this case,
 697 we observe a monotonic behavior, and the variations of the drag coefficient with \mathcal{L} are
 698 considerably smaller than those observed when varying \mathcal{F} . The distribution, at low values of
 699 $\mathcal{L} \approx 5 \times 10^{-3}$ shows a peak at $\alpha \approx 130^\circ$, that decreases with \mathcal{L} , and is negative in the other
 700 regions of the membrane.

701 In this section, we derived the sensitivity of the drag coefficient with respect to variations
 702 of \mathcal{F} and \mathcal{L} . In the following, we exploit the sensitivity analysis to introduce a gradient-based
 703 optimization for the geometry of the membrane, when both the filtrability and slip numbers
 704 are varied together, so as to find the optimal distribution of \mathcal{F} and \mathcal{L} to maximize the drag
 705 coefficient.

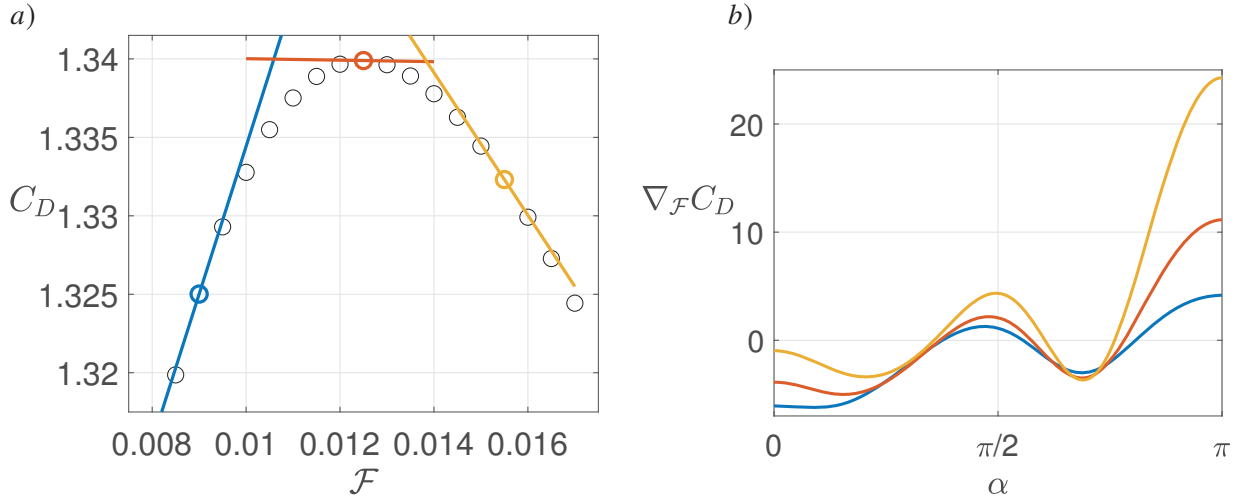


Figure 16: Panel *a*): variation of the drag coefficient with \mathcal{F} , for $\mathcal{L} = 5 \times 10^{-3}$, directly evaluated from macroscopic model (2.6, 2.7) (black circles) and predictions of the gradient via the sensitivity approach (coloured lines) carried out around the configurations identified by coloured circles. Panel *b*): distribution of sensitivity with respect to \mathcal{F} along the $y > 0$ part of the cylinder, i.e. $0 < \alpha < \pi$, for the configurations denoted with colors in panel *a*).

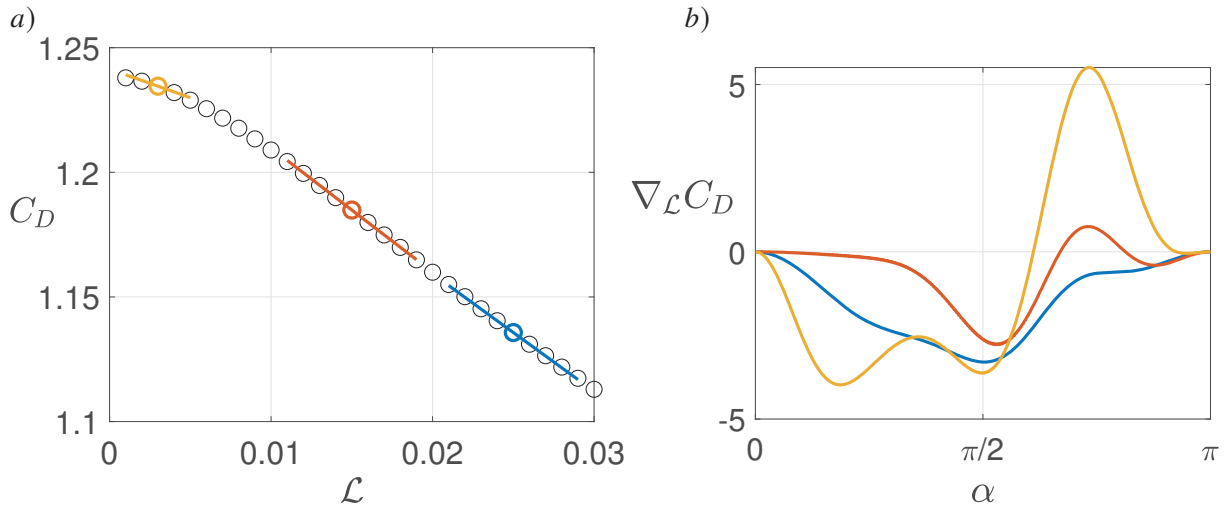


Figure 17: Panel *a*): variation of the drag coefficient with \mathcal{L} , for $\mathcal{F} = 0.03$, directly evaluated from macroscopic model (2.6, 2.7) (black circles) and predictions of the gradient via the sensitivity approach (coloured lines) carried out around the corresponding coloured circles. Panel *b*): distribution of sensitivity with respect to \mathcal{L} along the $y > 0$ part of the cylinder, $0 < \alpha < \pi$.

5.2. Optimal distribution of the properties of the membrane

707 The sensitivity functions found in the previous section are used here to obtain the optimal
 708 distributions of \mathcal{F} and \mathcal{L} that maximize the drag coefficient. The starting profiles of \mathcal{F}
 709 and \mathcal{L} for the gradient-based optimization are uniform. We chose different values of the
 710 initial guess, among which $\mathcal{F}^{(0)} = 1.25 \times 10^{-2}$ and $\mathcal{L}^{(0)} = 5 \times 10^{-3}$, i.e. the values that
 711 maximize C_D when the permeable membrane is formed by a repetition of a single microscopic
 712 inclusion (case denoted by the \square symbol in figure 12). We implement gradient-ascent iterative
 713 procedure, using as initial guess $\mathcal{F}^{(0)}$ and $\mathcal{L}^{(0)}$. At each iteration (i), the value of the gradients
 714 $\nabla_{\mathcal{F}}^{(i)} C_D$ and $\nabla_{\mathcal{L}}^{(i)} C_D$ are evaluated by the adjoint analysis proposed above. We thus update

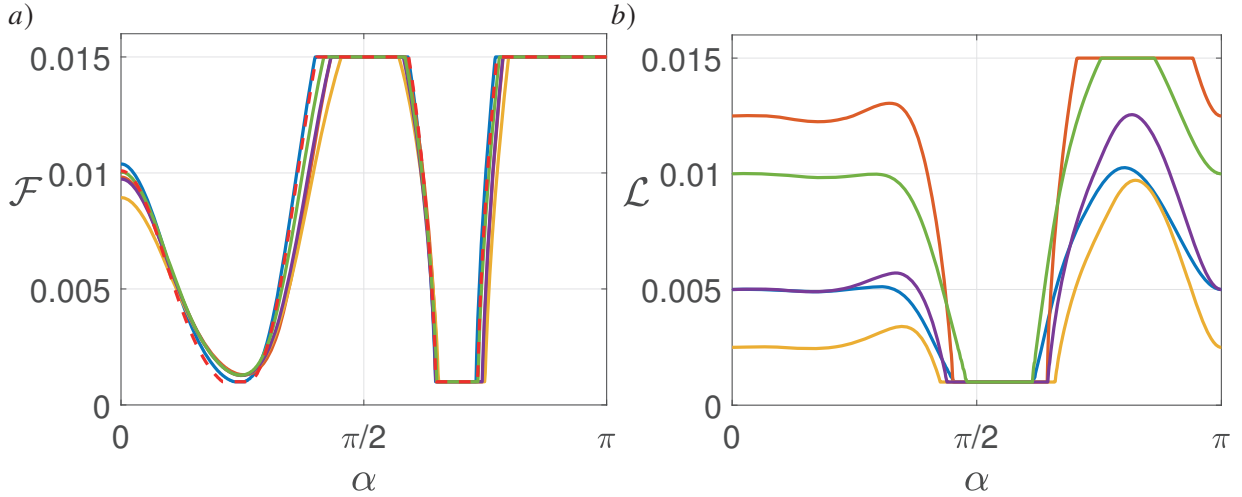


Figure 18: Results from the gradient-based optimization. Final distribution of (a) \mathcal{F} and (b) \mathcal{L} , when both \mathcal{F} and \mathcal{L} are optimized for different initial guesses (coloured lines) and when only variations of \mathcal{F} are considered with initial guess $\mathcal{F}^{(0)} = 0.0125$ and $\mathcal{L}^{(0)} = 0.005$ (red dashed line). The various initial guesses are $\mathcal{F}^{(0)} = 0.0125$ and $\mathcal{L}^{(0)} = 0.005$ (blue), $\mathcal{F}^{(0)} = 0.005$ and $\mathcal{L}^{(0)} = 0.0125$ (orange), $\mathcal{F}^{(0)} = 0.0025$ and $\mathcal{L}^{(0)} = 0.0025$ (yellow), $\mathcal{F}^{(0)} = 0.005$ and $\mathcal{L}^{(0)} = 0.005$ (purple), $\mathcal{F}^{(0)} = 0.01$, $\mathcal{L}^{(0)} = 0.01$ (green).

715 the distribution of \mathcal{F} and \mathcal{L} in the direction of the gradient as follows

$$716 \quad \mathcal{F}^{(i+1)} = \mathcal{F}^{(i)} + \nabla_{\mathcal{F}}^{(i)} C_D \delta \mathcal{F} \quad \text{and} \quad \mathcal{L}^{(i+1)} = \mathcal{L}^{(i)} + \nabla_{\mathcal{L}}^{(i)} C_D \delta \mathcal{L}, \quad (5.7)$$

717 with fixed step sizes $\delta \mathcal{F} = 10^{-2} \mathcal{F}^{(0)}$ and $\delta \mathcal{L} = 10^{-2} \mathcal{L}^{(0)}$. During the optimization procedure,
 718 the values of \mathcal{F} and \mathcal{L} have to remain strictly positive, to avoid non-physical values. Besides,
 719 too small or too large values jeopardize the inverse procedure, since large differences in the
 720 dimensions of the microscopic inclusions are difficult to handle without considering large
 721 values of the parameter ε , which degrade the accuracy of the homogenized model. Typical
 722 procedures to regularize the problem are based on the introduction of auxiliary variables
 723 to transform the inequality conditions into equality ones (Schulze & Sesterhenn 2013), or
 724 on the truncation of the gradient when the threshold values are reached (Lin 2007). In this
 725 work, for the sake of simplicity, we apply the latter procedure and we restrict the research
 726 of the optimal profiles to the intervals $10^{-3} < \mathcal{F}, \mathcal{L} < 1.5 \times 10^{-2}$. At each iteration, values
 727 of \mathcal{F} or \mathcal{L} larger (resp. lower) than the threshold value, due to an increase (resp. decrease)
 728 along the gradient direction, are imposed to be equal to the threshold value. The iterative
 729 procedure is stopped when the relative difference between two successive evaluations of the
 730 drag coefficient is less than 10^{-4} .

731 In figure 18 we report the optimal distribution of \mathcal{F} and \mathcal{L} along the semi-cylinder found
 732 via the iterative algorithm, for the optimization with both \mathcal{F} and \mathcal{L} , with different initial
 733 guesses. Note that, depending on the initial value, a different number of iterations is needed to
 734 achieve convergence. While the final distribution of \mathcal{F} does not show significant variations
 735 with the initial guess, the profiles of \mathcal{L} are different. In the rear part, $0 < \alpha < \pi/2$, \mathcal{L}
 736 remains constant and equal to the initial value. For $\alpha \approx \pi/2$, all distributions collapse to
 737 the lower threshold value, and in the front part they assume different values. However, the
 738 effect of the slip number on the final value of the drag coefficient (figure 19a) is small and
 739 the differences are below 0.5%. Therefore, the effect of the filtrability is predominant and
 740 the optimal distribution of \mathcal{F} is weakly influenced by \mathcal{L} . We thus consider the case in which
 741 the slip number is kept fixed, while the optimization is performed only on \mathcal{F} . The resulting

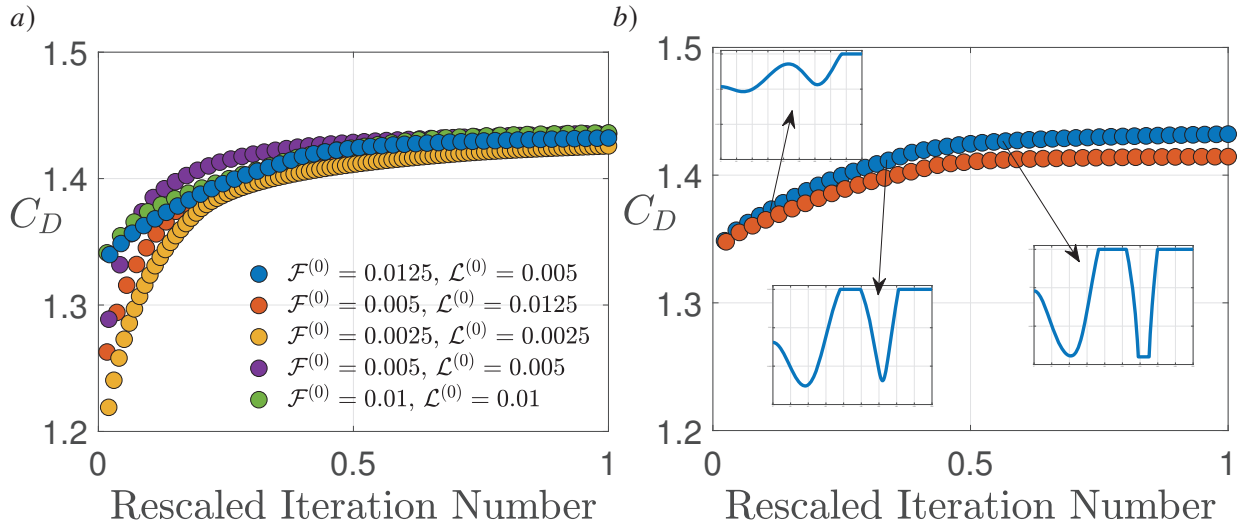


Figure 19: (a) Variation of the drag coefficient during the optimization procedure, for different initial guesses, as a function of the iteration number rescaled by the total number of iterations required to reach convergence. (b) Variation of the drag coefficient during the iterative procedure of the gradient-based optimization, when both \mathcal{F} and \mathcal{L} (blue dots) and only \mathcal{F} (orange dots) are varied, with initial guess $\mathcal{F}^{(0)} = 0.0125$ and $\mathcal{L}^{(0)} = 0.005$. In the insets, we report the distributions of \mathcal{F} for different iterations, the horizontal and vertical axes of the insets correspond to $0 < \alpha < \pi$ and $0 < \mathcal{F} < 1.55 \times 10^{-2}$, respectively.

742 distribution (red dashed line in figure 18a) is very similar to the other ones optimized both
 743 with respect to \mathcal{F} and \mathcal{L} . Both approaches converge to a similar value of C_D (figure 19b),
 744 which is $\approx 6\%$ larger than the maximum drag obtained with uniform membrane properties.
 745 We therefore conclude that the optimization procedure leads to significantly larger values of
 746 C_D , in which the effect of the filtrability is predominant, with a weak dependence on the
 747 initial guess.

748 The increase of drag in the optimal configuration can be related to the previous observations
 749 in the case of constant filtrability. The optimization procedure tends to increase the filtrability
 750 in the front part ($\alpha \approx \pi$) of the cylinder and at $\alpha \approx \pi/2$, while it tends to decrease it at $\alpha \approx \pi/4$
 751 and $\alpha \approx (3/4)\pi$. Compared to the constant filtrability case, the curvature of the streamlines is
 752 enhanced, thus leading to a more marked recompression in the inner part of the downstream
 753 portion of the membrane. This effect, leading to an increase of global drag, is enhanced in
 754 the optimal configuration since the flow is more constrained to pass through the front and
 755 the streamlines leave the cylinder through a narrower region, at $\alpha \approx \pi/2$, owing to the large
 756 values of filtrability in these regions. This constraint further magnifies the effects of the inner
 757 pressure gradients presented in the constant properties case. The analysis of the distributions
 758 of slip number shows that the drag is not influenced by variations of slip in the rear part of
 759 the cylinder.

760 In this section, we performed an adjoint-based optimization of the flow with respect to the
 761 drag. The typical computational time for one step of the optimization is equivalent to the
 762 one of a steady calculation of the non-linear Navier-Stokes equations, i.e. around one minute
 763 for a common laptop computer. Since on average 30-60 iterations were needed to achieve
 764 convergence, with the presented simple algorithm, one optimization lasts for 30-60 minutes.
 765 The decoupling between microscopic properties and macroscopic effects on the flow allows
 766 one to move from a generic shape optimization problem to an optimization problem for the
 767 two scalar distributions $\mathcal{F}(\alpha)$ and $\mathcal{L}(\alpha)$, making the optimization procedure straightforward
 768 to implement compared to a full-scale case. Once the distribution of membrane properties is
 769 known, the inverse procedure has to be applied to choose the microscopic structure. In the

770 following, we aim at retrieving an optimal full-scale structure of the membrane starting from
 771 the optimal profile of \mathcal{F} found in the present section.

772 6. Full-scale design of membranes of variable properties

773 In order to fulfill the inverse procedure introduced in figure 3, we link the optimal distribution
 774 of filtrability and slip found in Section 5.2 to a real full-scale structure of the permeable shell
 775 where the microscopic solid inclusions vary in shape and/or size. Since the effective stress
 776 jump condition developed by Zampogna & Gallaire (2020) has not been initially thought for
 777 membranes formed by solid inclusions of variable shape along the membrane, the first step
 778 to reach our objective is to modify and prove the validity of the macroscopic model for this
 779 case.

780 6.1. Application of the effective stress jump model to the case of membranes with 781 fast-varying microscopic geometry

782 The easiest way to compute the microscopic tensors within the homogenization framework
 783 consists of assuming that the solid structure consists of a periodic repetition of a given unit
 784 cell (cf. for a review Hornung 1997). To relax this assumption one may assume that the
 785 variations of the microscopic structure are slow (cf., for instance, Dalwadi *et al.* 2016) and
 786 hence solve the microscopic periodic problems (4.1) and (4.2) over each periodic unit cell and
 787 then compute the effective macroscopic tensors by averaging the microscopic solution over
 788 each cell. In the context of the present work, since fast variations of \mathcal{F} and \mathcal{L} can be noticed
 789 in the optimal distributions of figure 18, we need a model to link the effective properties to
 790 the microscopic geometry, without any assumption about the nature of the variations of the
 791 inclusions along the membrane. The macroscopic model of Zampogna & Gallaire (2020) is
 792 adapted here so as to describe this case when the following hypotheses are valid:

- 793 • the permeable shell is the surface of a rotational body, whose radius is R ;
- 794 • the constraint $\ell/D \ll 1$ is still valid.

795 Under such assumptions, the macroscopic curvature is neglected in the microscopic domain
 796 as also done in Zampogna & Gallaire (2020) and the microscopic problems (4.1) and (4.2)
 797 are solved in the entire cylindrical shell, \mathbb{F}_{tot} , sketched in figure 20b, defined as

$$798 \quad \mathbb{F}_{tot} = \cup_{i=1}^N \mathbb{F}_i, \quad (6.1)$$

799 where \mathbb{F}_i is the fluid domain within the i -th unit cell sketched in figure 20b and N the
 800 total number of solid inclusions on the shell. On the left and right sides of \mathbb{F}_{tot} , we impose
 801 periodic boundary conditions as we are dealing with the surface of a rotational body. With
 802 these modifications, i.e. solving the microscopic problems (4.1) and (4.2) over \mathbb{F}_{tot} instead of
 803 over each \mathbb{F}_i , the assumption of slow variations of the microscopic geometry is superfluous
 804 and a fast-varying microscopic geometry can be studied and associated with the optimal
 805 profile of \mathcal{F} found in the previous subsection.

806 To validate the model, we first calculate the microscopic quantities associated with two
 807 different distributions of solid inclusions along the membrane, D1 and D2. They represent
 808 an example of slow- (D1) and fast-varying (D2) microscopic geometries (cf. table 3). The
 809 distribution D1 is represented in the Cartesian frame of reference in figure 20a and in the
 810 local frame of reference of the cylinder in figure 20b. The values of \mathcal{F} and \mathcal{L} for distributions
 811 D1 and D2 are shown in figures 21a and 21b, respectively. While blue stars represent the
 812 values extracted from the solutions computed within \mathbb{F}_{tot} by averaging over each unit cell, the
 813 light-blue circles represent the values of \mathcal{F} and \mathcal{L} deduced by classical calculations over each
 814 periodic unit cell \mathbb{F}_i . In the case of slow variations of the microscopic structure, the periodic
 815 problems (4.1) and (4.2) over the unit cell provide acceptable results for the effective tensors.

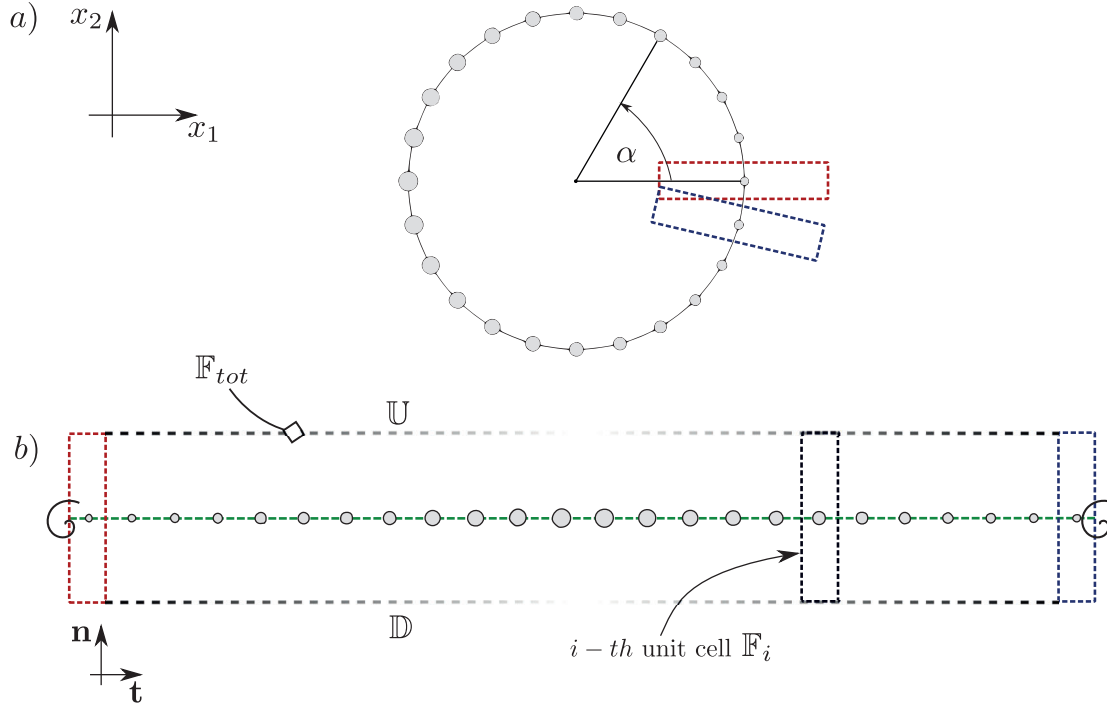


Figure 20: Panel a): example of a cylindrical shell formed by variable microscopic inclusions, corresponding to distribution D1 in table 3. Panel b): sketch of the microscopic domain, \mathbb{F}_{tot} , built by “unrolling” the cylindrical shell (red and blue unit cells correspond to their “rolled” counterpart in panel a). In order to deduce averaged profiles of F_n and L_t the solution is averaged within each cell over the green dashed line.

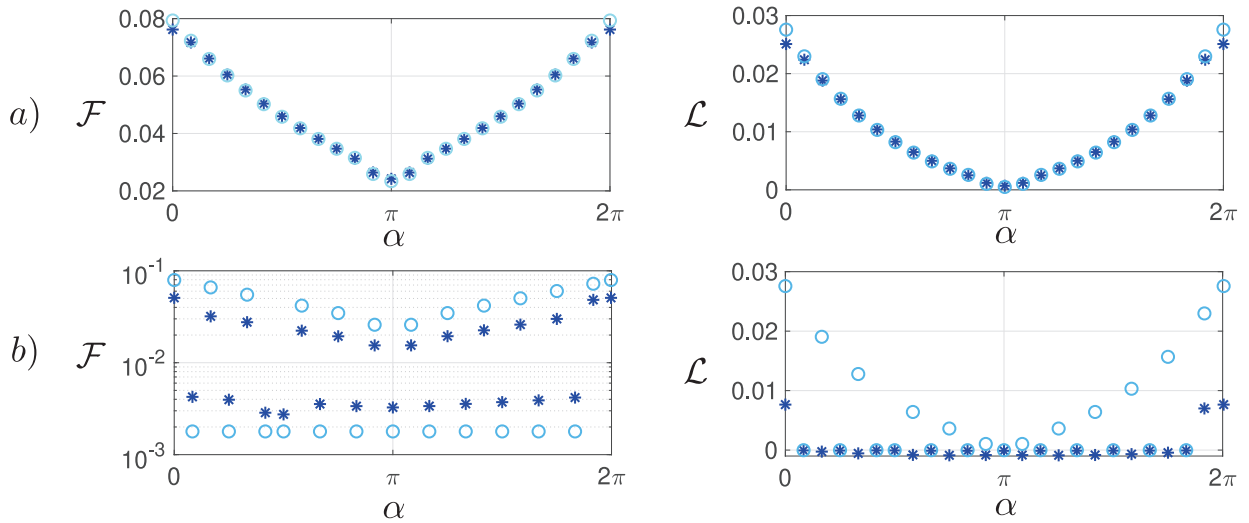


Figure 21: Values of \mathcal{F} and \mathcal{L} along \mathbb{F}_{tot} (blue stars) and corresponding values computed within each cell \mathbb{F}_i (light-blue circles) for distributions D1 (panel a) and D2 (panel b) described in table 3.

816 Conversely, the important discrepancies between the blue and light-blue profiles represented
 817 in panel b) show that fast-variations of the microscopic geometries affect in a relevant way
 818 the values of the effective quantities \mathcal{F} and \mathcal{L} and microscopic problems (4.1) and (4.2) have
 819 to be computed over the entire microscopic domain \mathbb{F}_{tot} .

820 The last statement is supported by the comparison between the full-scale and the equivalent
 821 model that can be done once the effective values of \mathcal{F} and \mathcal{L} have been found. As shown in
 822 figure 22, the macroscopic velocities evaluated over the membrane are in perfect agreement
 823 with the full-scale profile for the case D1 of slow-varying geometries. The drag coefficient

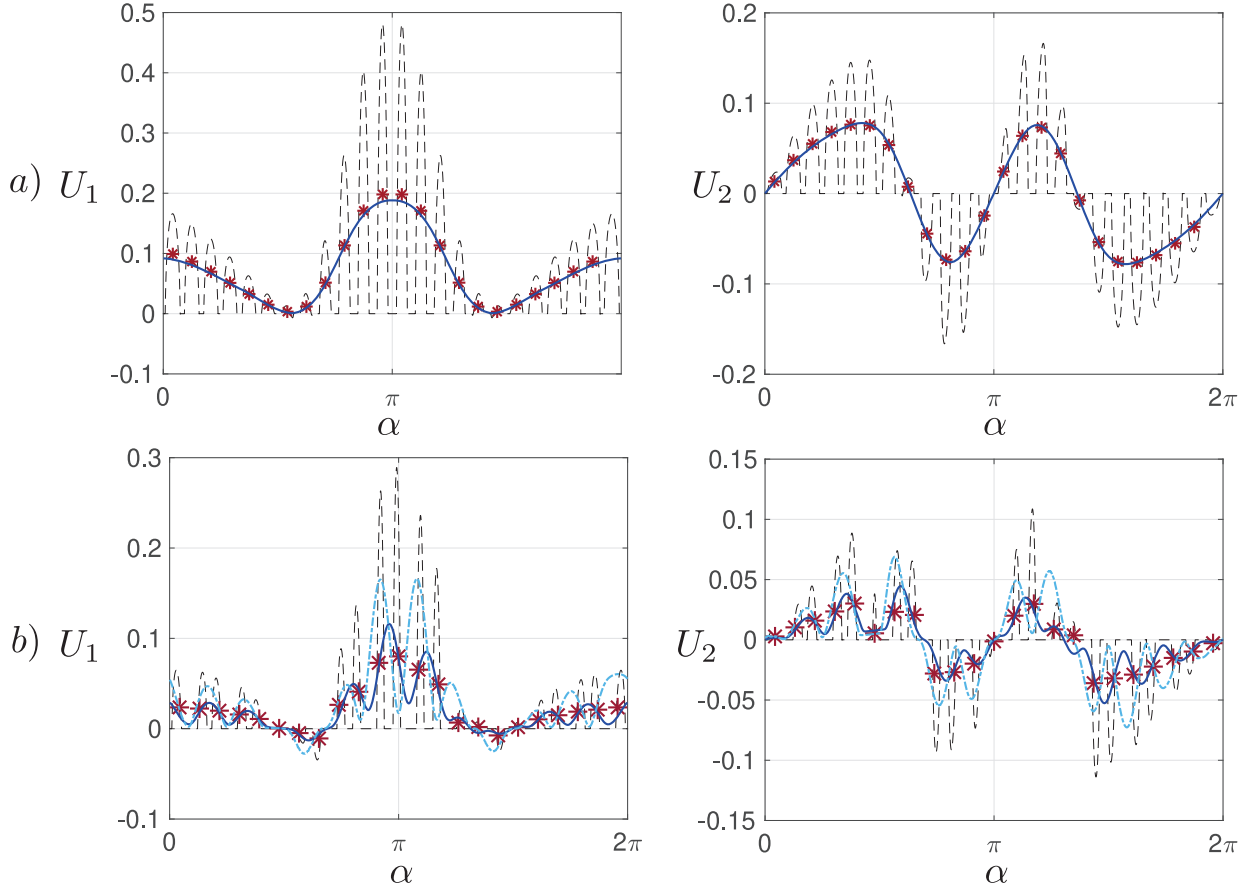


Figure 22: Comparison between the full-scale solution and the macroscopic model for distribution D1 and D2 (panels *a* and *b* respectively). All quantities are evaluated over the equivalent membrane Γ_{int} . Dashed lines represent the full-scale model, blue lines the macroscopic model where the values of the effective tensors have been calculated in \mathbb{F}_{tot} , light-blue dot-dashed lines correspond to the macroscopic model where the values of the effective tensors have been calculated in each periodic unit cell \mathbb{F}_i and red stars are the average of the full-scale model.

824 computed from the equivalent solution, C_D^{EQ} , is equal to 1.225, with a relative error with
 825 respect to the full-scale solution of $\approx 1.5\%$, in the order of the approximation. No substantial
 826 differences are noticed using the values of the effective tensor extracted from \mathbb{F}_{tot} or from
 827 each periodic unit cell \mathbb{F}_i . On the contrary, when distribution D2 is considered (figure 22*b*),
 828 the use of the effective tensor calculated within \mathbb{F}_{tot} allows us to drastically reduce the error
 829 between the full-scale simulation and the macroscopic model.

830 6.2. Retrieving the full-scale microscopic geometry from the optimal \mathcal{F} - \mathcal{L} -profiles

831 In the previous paragraph we showed that the effective stress jump condition of Zampogna &
 832 Gallaire (2020) is reliable also in the case of fast-varying microscopic geometries when the
 833 adequate precautions described above are taken into account to formulate the microscopic
 834 problems (4.1, 4.2). We thus apply it to link the optimal distributions of effective filtrability
 835 and slip profiles found in Section 5.2 to a distribution of microscopic solid inclusions in
 836 order to design an optimal cylindrical membrane for drag maximization. For the sake of
 837 simplicity, we consider the case in which the optimization procedure is performed only on
 838 the value of \mathcal{F} , letting \mathcal{L} vary accordingly to the microscopic calculations. This allows us to
 839 focus our attention only on circular (rather than elliptical) inclusions of variable radius. As a
 840 consequence, the profile of \mathcal{L} is unequivocally defined once the \mathcal{F} profile is retrieved. This
 841 simplifying assumption has a marginal effect on the resulting optimal drag since the latter is

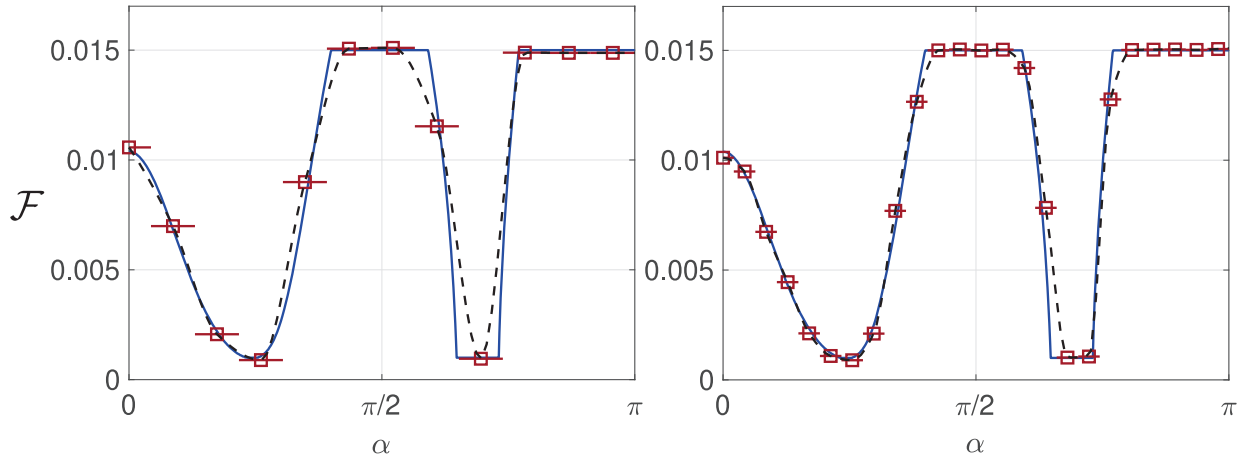


Figure 23: Variation of the optimal \mathcal{F} -profile with α . Blue lines correspond to the values of \mathcal{F} found in Section 5.2 while red squares to the values of \mathcal{F} reconstructed from the microscopic problems in \mathbb{F}_{tot} . Black dashed lines correspond to the profiles reconstructed via a piecewise cubic interpolation of the red square-profile. In the left panel 23 inclusions have been placed on the cylindrical shell ($\varepsilon = 0.1369$) while on the right one 47 inclusions have been used ($\varepsilon = 0.0667$). A larger number of inclusions allows us to better reconstruct the \mathcal{F} profile.

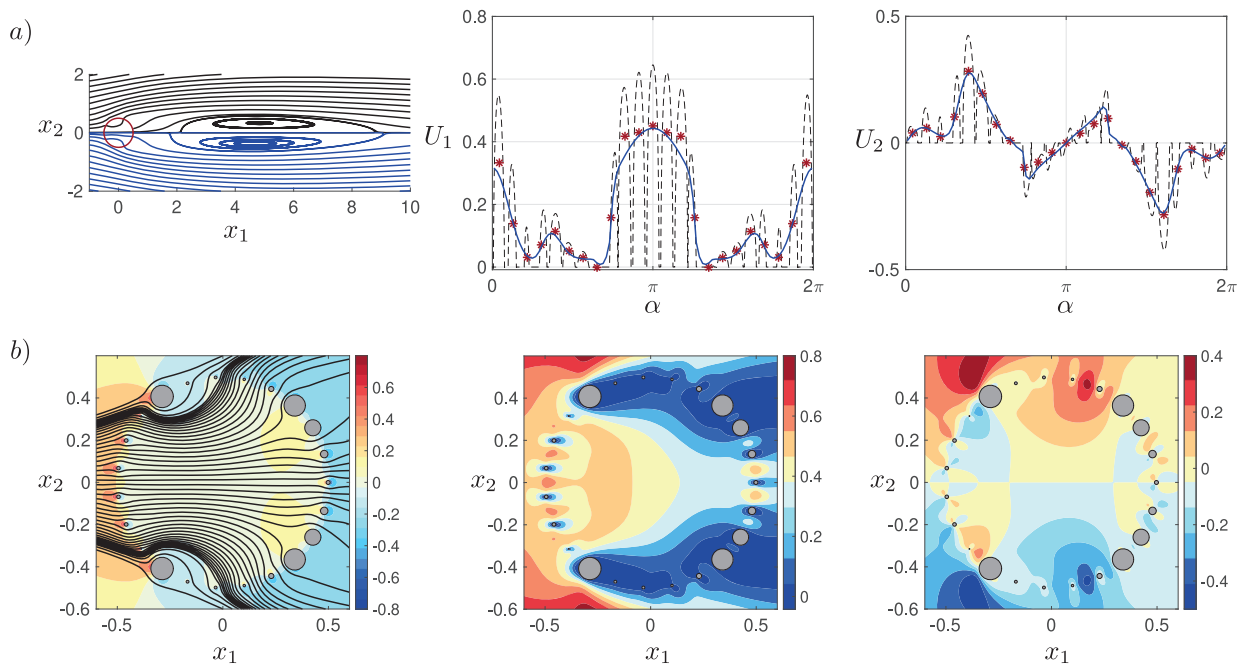


Figure 24: Flow past the optimal cylindrical structure deduced from the profile of \mathcal{F} computed in Section 5.2. A total number of 23 solid inclusions (sketched in dark gray in panel *b*) have been placed on the cylinder leading to a value of ε equal to 0.137. Top row: comparison between full-scale and macroscopic solution. In the left panel the flow streamlines for the full-scale simulation (black lines) and for the macroscopic model (blue lines). In the central and right panels the horizontal and vertical velocities are represented over Γ_{int} . Black dashed lines represent the full-scale solution, blue lines the macroscopic model, where \mathcal{F} and \mathcal{L} are evaluated using the reconstructed profiles (cf. figure 23), and red stars the averaged full-scale profile. Bottom row: isocontours of pressure (left panel), horizontal (center panel) and vertical velocity (right panel) around the cylindrical shell. In the left panel also flow streamlines within the shell have been represented to better appreciate the flow behavior.

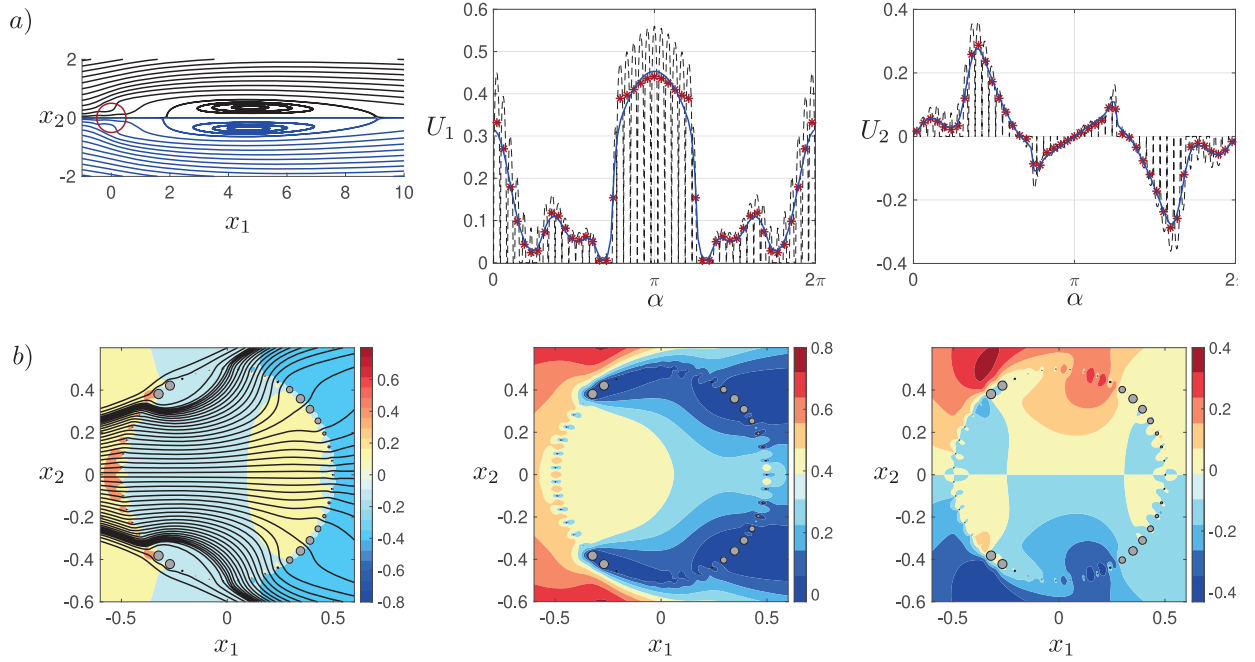


Figure 25: Same as figure 24 for a total number of 47 solid inclusions on the cylinder, leading to $\varepsilon = 0.066$.

842 only weakly affected by \mathcal{L} . Nevertheless, the following procedure can be straightforwardly
 843 generalized to variable distributions of both \mathcal{F} and \mathcal{L} , by considering for instance elliptical
 844 inclusions as in Section 4.2. The numerical implementation is based on a bisection method
 845 (see Appendix C), where at each iteration the value of the radius of each inclusion is
 846 adjusted so as to reach the aimed values of \mathcal{F} up to a relative tolerance of 1%. For the
 847 iterative procedure to be well defined, an initial guess has to be taken. A good candidate
 848 is the value of \mathcal{F} given by the case of perfectly periodic microstructures. The separation
 849 of scales parameter ε is a free parameter and has to be chosen to unequivocally define the
 850 radius of the solid inclusions. The resulting distributions are sketched in figure 23 for two
 851 different values of $\varepsilon = 0.1369, 0.0667$, corresponding to 23 and 47 solid inclusions over the
 852 cylinder, respectively. We reconstruct the continuous \mathcal{F} and \mathcal{L} profiles via a piecewise-cubic
 853 interpolation (black dashed lines in figure 23) of the piecewise constant values obtained
 854 from the solution of the microscopic problems averaged in each unit cell (red squares);
 855 however, we verified that the following results were not affected by a different choice of the
 856 interpolation. As last check, we perform macroscopic and full-scale simulations in order to
 857 *i)* confirm the validity of the model in this case and *ii)* check that the full-scale geometry
 858 actually maximizes the drag coefficient, as predicted in the Lagrangian-based optimization
 859 procedure. Figures 24 and 25 provide qualitative and quantitative information about the flow
 860 past the two retrieved full-scale optimal structures. According to panel a) of those figures,
 861 for both values of ε the full-scale solution reproduces well the behavior and properties of the
 862 macroscopic flow calculated using the optimal profile of \mathcal{F} . The drag coefficients calculated
 863 over the two full-scale structures are $C_D^{\varepsilon=0.1369} = 1.427$ and $C_D^{\varepsilon=0.0667} = 1.412$, while the
 864 corresponding one estimated by the macroscopic model is equal to 1.414, exhibiting an error
 865 of about 1% in the worst case. The variability of the microscopic inclusions is shown in
 866 panel b) of figures 24 and 25, where a focus on the pressure and velocity fields across the
 867 cylindrical shell reveals the presence of local microscopic flow structures that become less
 868 and less important as ε decreases. We refer to table 3 for the geometrical data used to build
 869 each full scale structure and to figure 28 for their visualization.

870 These last findings accomplish the procedure sketched in figure 3. As previously shown,

871 the inverse procedure admits multiple solutions, whose number can be further reduced by
872 imposing other kinds of geometrical or functional constraints to the problem considered.

873 **7. Conclusions and perspectives**

874 In this work, we proposed an approach for the *homogenization-based optimization of*
875 *permeable membranes*. We considered as a test case the wake flow past a permeable
876 circular cylinder. The first part of the procedure was a parametric study of the steady
877 flow configurations and their stability with respect to perturbations. In this framework,
878 the membrane was modeled by the effective stress jump interface condition developed in
879 Zampogna & Gallaire (2020), for symmetric configurations with respect to the centerline
880 of the membrane. Under these conditions, the membrane properties are described by two
881 scalars, the filtrability and the slip numbers, the former representing the ability of the fluid
882 to pass through the membrane while the latter its ability to flow along the tangential-to-the-
883 membrane direction. The flow morphology strongly resembles the one outlined in Ledda
884 *et al.* (2018). The recirculation region past the cylinder detaches from the body and moves
885 downstream, becomes smaller and disappears, as the filtrability number was increased.
886 An increase in the slip number showed a decrease in the dimensions of the recirculation
887 region. Interestingly, for large values of the filtrability number, the drag coefficient presents a
888 maximum that is substantially larger than the drag coefficient of an impermeable cylinder. A
889 bifurcation diagram was identified via the stability analysis, which unraveled the stabilization
890 of the steady wake for large values of filtrability, a situation similar to the one outlined in
891 Ledda *et al.* (2018). The unstable mode leads to a vortex shedding whose onset region moves
892 downstream as the filtrability is increased.

893 Once the unstable configurations were excluded from the analysis, the second part of
894 the work was focused on the reconstruction of the membrane based on the values of
895 filtrability and slip numbers, identified to obtain proper macroscopic characteristics of the
896 flow. We considered different test cases, among which the conditions that maximize the drag
897 coefficient. We also outlined a procedure to recover the microscopic geometry that satisfies the
898 constraints of filtrability and slip numbers, for elliptical inclusions. The agreement between
899 the homogenized model and the full-scale simulations was very good, proving not only
900 the faithfulness of the inverse procedure, but also the accuracy of the effective stress jump
901 condition which was initially tested in Zampogna & Gallaire (2020) only in the Stokes flow
902 regime.

903 The third part of the work was devoted to the optimization of a membrane whose filtrability
904 and slip numbers were allowed to vary along the cylinder and to the reconstruction of the
905 corresponding microscopic structure. As a test case, we considered as optimal objective
906 the maximization of the drag coefficient. We first evaluated the sensitivity with respect
907 to variations of the filtrability and slip numbers and thus performed a gradient-ascent
908 optimization, using as initial guess the values of filtrability and slip numbers that maximize
909 the drag in the case of constant membrane properties. In this test case, we obtained an
910 increase in the drag coefficient of 6% with respect to the case with constant membrane
911 properties, and thus of 34% with respect to the solid case. We then introduced a procedure to
912 recover the microscopic structure that satisfies an optimal filtrability distribution, focusing on
913 circular inclusions. The introduction of a new modified domain of validity of the microscopic
914 problems associated with filtrability and slip numbers allowed us to correctly link these
915 quantities to a full-scale geometry. Also in this case the agreement was fully satisfactory, thus
916 validating the proposed approach both for constant and variable distributions of filtrability
917 and slip numbers along the membrane.

918 This work aims at giving a rationale to the application of homogenized models to design

919 membranes in the context of flow control, providing fast and accurate predictions and the
 920 opportunity to directly link macroscopic characteristics of the membrane to microscopic
 921 geometries. Thanks to the generality of the macroscopic model, real three-dimensional
 922 permeable shells can be handled at the cost of adding only one more parameter, representing
 923 the ability of the fluid to flow along the second tangent-to-the-membrane direction, much
 924 lower than the cost of adding approximately $1/\varepsilon$ degrees of freedom due to the meshing of
 925 a real full-scale three-dimensional membrane. The potential of the method stems from the
 926 decoupling between microscopic properties and macroscopic effects on the flow, which
 927 allows one to have a plethora of possible microscopic configurations giving the same
 928 macroscopic flow. This decoupling drastically simplifies the adjoint-based optimization
 929 procedure, allowing to obtain a single distribution of membrane properties which can
 930 be satisfied by an infinite number of possible microscopic geometries; the number of
 931 corresponding microscopic geometries can be further reduced by imposing other constraints.
 932 Despite the theoretical and analytical complexity of the homogenization technique, the final
 933 result consists of a simple boundary condition for the macroscopic flow model that enables
 934 to explore a vast range of geometrical configurations, with the great advantage of a drastic
 935 reduction of the complexity and computational times needed to carry out the solution.

936 This work may be extended in several ways. The procedure explained here is a first step
 937 towards a rational design of membranes; if integrated with a model describing the equivalent
 938 transport of diluted substances across a permeable wall it represents a potential answer to
 939 the necessity identified in Park *et al.* (2017) to find the right balance of filtrability between
 940 a fluid and a diluted substance. The comparisons considered in the present paper show that
 941 the homogenized model well reproduces the flow behavior in the case of inertial flows. The
 942 differences with respect to the full-scale solution are larger for cases in which the microscopic
 943 Reynolds number, $Re_{micro} = U\ell/\nu$, is large (cf. for instance the case denoted by \bigcirc in table 1
 944 where $Re_{micro} \approx 25$). This pushes us to proceed toward an extension of the model for high-
 945 Re flows, where the inertia of the flow within the membrane cannot be neglected (Zampogna
 946 & Bottaro 2016).

947 We conclude by observing that the interweaving of homogenization theory, bifurcation
 948 analysis and adjoint optimization methods showed great potential, opening up the path to a
 949 rational design of complex structures that can find a wide and varied range of applications
 950 in fluid dynamics.

951 **Funding.** This work was supported by the Swiss National Science Foundation (grant no.
 952 200021_178971 to P.G.L. and grant no. 514636 to G.A.Z). F.G. and G.A.Z. acknowledge the
 953 EuroTech Postdoc Programme, co-funded by the European Commission under its framework
 954 programme Horizon 2020, (grant agreement no. 754462).

955 **Declaration of Interests.** The authors report no conflict of interest.

956 Appendix A. Mesh convergence

957 In this section, we report the results of the mesh convergence. We considered the case
 958 $Re = 100$, $\mathcal{F} = 1.25 \times 10^{-2}$ and $\mathcal{L} = 5 \times 10^{-3}$. We verified both the convergence with respect
 959 to the size of the domain and with respect to the number of elements. The results are reported
 960 in Table 2, for the drag coefficient and for the unstable eigenvalue studied in Section 3.2.
 961 We initially increased the number of elements for the mesh $M1$, verifying the convergence.
 962 We therefore increased the domain size to verify its effect. We conclude that the number of
 963 elements and the size of the domain have a small impact on the baseflow and global stability

Mesh	x_{1in}	x_{1out}	x_{2lat}	N_1	N_2	N_3	N_4	N_{int}	No. Elements	C_D	$\text{Re}(\lambda)$	$\text{Im}(\lambda)$
$M1$	-30	90	25	1	1.25	5	13.3	31.9	144008	1.339894	-0.03687	0.71985
$M2$	-30	90	25	1.25	1.55	6.3	16.7	39.8	161896	1.339888	-0.03685	0.71980
$M3$	-30	90	25	1.5	1.9	7.5	20	47.8	187498	1.339888	-0.03678	0.71986
$M4$	-30	90	25	2	2.5	10	26.7	63.7	241094	1.339886	0.03673	0.71999
$M1B$	-45	120	37.5	1	1.25	5	13.3	31.9	164918	1.333833	-0.03831	0.71867
$M1C$	-60	180	50	1	1.25	5	13.3	31.9	193202	1.334047	-0.03843	0.71878

Table 2: Results of the mesh convergence. The edge densities are denoted with N , for different regions as depicted in figure 2.

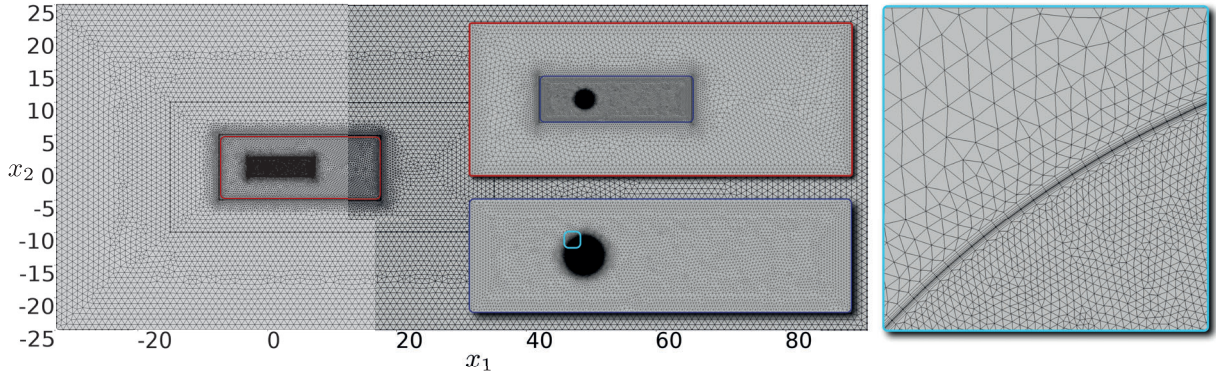


Figure 26: Overview of the mesh denoted by $M1$ in table 2 used for the macroscopic computations. In each colored inset recursive magnifications approaching the cylinder are shown. In the light-blue inset prismatic layers adjacent to the fictitious interface Γ_{int} can be noticed; they have been added in order to well evaluate the normal-to-the-membrane fluid stress and integral quantities like the drag force acting on the cylinder.

964 results, two significant digits remaining constant for every measured quantity. The mesh $M1$
965 (shown in figure 26) is suitable for the study and it has been used throughout the work.

966 Appendix B. Derivation of the sensitivity of the drag coefficient with respect to 967 variations of the membrane properties

968 We propose here an extensive derivation of the sensitivity functions briefly introduced in
969 Section 5.2. For the sake of clarity, we recall that, at the interface, we denote with the
970 superscripts \cdot^+ and \cdot^- the following limits

$$971 \quad f^- = \lim_{x_i \rightarrow \Gamma_{int}^-} f \quad \text{and} \quad f^+ = \lim_{x_i \rightarrow \Gamma_{int}^+} f, \quad (\text{B } 1)$$

972 with Γ_{int}^- and Γ_{int}^+ the outer and inner sides of Γ_{int} . The drag coefficient, i.e. the objective
973 in the Lagrangian framework, is defined in equation (5.1). According to this equation, any
974 small modification of the tensor component \mathcal{M}_{ij} modifies the drag by δC_D according to

$$975 \quad \delta C_D = 2 \oint_{\Gamma_{cyl}} (\Sigma_{jk} (\delta p^-, \delta \mathbf{u}^-) - \Sigma_{jk} (\delta p^+, \delta \mathbf{u}^+)) n_k \delta_{1j} d\Gamma = \oint_{\Gamma_{cyl}} \nabla_{\mathcal{M}_{ij}} C_D \delta \mathcal{M}_{ij} d\Gamma, \quad (\text{B } 2)$$

976 where $(\delta \mathbf{u}^\pm, \delta p^\pm)$ is the linear perturbation to the base solution induced by the variation
977 of the membrane tensor, whose governing equations can be deduced by substituting the
978 perturbed variables ($\mathbf{u} = \mathbf{U} + \delta \mathbf{u}$, $p = P + \delta p$) in equations (2.6, 2.7) and read

$$\begin{aligned}
& \partial_i \delta u_i = 0, \quad \delta u_j \partial_j U_i + U_j \partial_j \delta u_i = -\partial_i \delta p + \frac{1}{Re} \partial_{jj}^2 \delta u_i \quad \text{in } \Omega \\
& \delta u_i^+ = \delta u_i^- = \delta u_i \quad \text{on } \Gamma_{\text{int}} \\
979 \quad \delta u_i = Re \mathcal{M}_{ij} (\Sigma_{jk} (\delta p^-, \delta \mathbf{u}^-) - \Sigma_{jk} (\delta p^+, \delta \mathbf{u}^+)) n_k + \\
& \quad + Re \delta \mathcal{M}_{ij} (\Sigma_{jk} (p^-, \mathbf{u}^-) - \Sigma_{jk} (p^+, \mathbf{u}^+)) n_k \quad \text{on } \Gamma_{\text{int}}, \tag{B 3}
\end{aligned}$$

980 together with boundary conditions $\delta u_i = 0$ at the inlet and $\Sigma_{jk} (\delta p, \delta \mathbf{u}) n_k = 0$ at the outflow.

981 We introduce the Lagrange multipliers $(\mathbf{u}^\dagger, p^\dagger, \mathbf{u}^{\dagger\dagger})$ referred to as the adjoint solution, and
982 define the functional

$$\begin{aligned}
\mathcal{J}(\mathbf{u}, p, \mathbf{u}^\dagger, p^\dagger, \mathbf{u}^{\dagger\dagger}, \mathcal{M}) = & C_D \\
& - \int_{\Omega} p^\dagger \partial_i u_i d\Omega \\
& - \int_{\Omega} u_i^\dagger (u_j \partial_j u_i - \partial_j \Sigma_{ij} (p, \mathbf{u})) d\Omega \\
& - \oint_{\Gamma_{\text{int}}} u_i^{\dagger\dagger} [u_i - Re \mathcal{M}_{ij} (\Sigma_{jk} (p^-, \mathbf{u}^-) - \Sigma_{jk} (p^+, \mathbf{u}^+)) n_k] d\Gamma, \\
983 & \tag{B 4}
\end{aligned}$$

984 whose gradient with respect to any variable f is

$$985 \quad \frac{\partial \mathcal{J}}{\partial f} \delta f = \lim_{\epsilon \rightarrow 0} \frac{\mathcal{J}(f + \epsilon \delta f) - \mathcal{J}(f)}{\epsilon}. \tag{B 5}$$

986 The variation of the drag coefficient thus reads:

$$987 \quad \delta C_D = \frac{\partial \mathcal{J}}{\partial (\mathbf{u}, p)} \delta (\mathbf{u}, p) + \frac{\partial \mathcal{J}}{\partial \mathcal{M}_{ij}} \delta \mathcal{M}_{ij}, \tag{B 6}$$

988 since the gradient of the functional with respect to the adjoint variable is zero as long as the
989 state equation is satisfied. The gradient with respect to (\mathbf{u}, p) is

$$\begin{aligned}
\frac{\partial \mathcal{J}}{\partial (\mathbf{u}, p)} \delta (\mathbf{u}, p) = & 2 \oint_{\Gamma_{\text{int}}} (\Sigma_{ij} (\delta p^-, \delta \mathbf{u}^-) - \Sigma_{ij} (\delta p^+, \delta \mathbf{u}^+)) n_j \delta_{1i} d\Gamma \\
& - \int_{\Omega} p^\dagger \partial_i \delta u_i d\Omega \\
& - \int_{\Omega} u_i^\dagger (U_j \partial_j \delta u_i + \delta u_j \partial_j U_i - \partial_j \Sigma_{ij} (\delta p, \delta \mathbf{u})) d\Omega \\
& - \oint_{\Gamma_{\text{int}}} u_i^{\dagger\dagger} [\delta u_i^- - Re \mathcal{M}_{ij} (\Sigma_{jk} (\delta p^-, \delta \mathbf{u}^-) - \Sigma_{jk} (\delta p^+, \delta \mathbf{u}^+)) n_k] d\Gamma \\
990 & \tag{B 7}
\end{aligned}$$

991 Integrating by parts and using the divergence theorem, we obtain analogous boundary terms

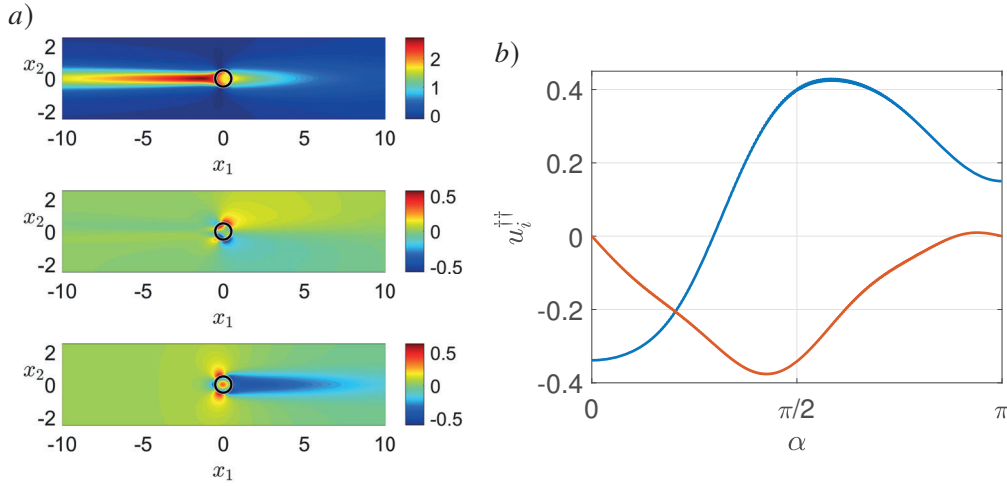


Figure 27: Adjoint field for $Re = 100$, $\mathcal{F} = 1.25 \times 10^{-2}$, $\mathcal{L} = 5 \times 10^{-3}$. Panel a): from top to bottom, u_1^\dagger , u_2^\dagger , p^\dagger . Panel b): $u_1^{\dagger\dagger}$ (blue curve) and $u_2^{\dagger\dagger}$ (orange curve) evaluated over Γ_{int} for $\alpha \in [0, \pi]$.

992 at Γ_{int} for the inner and outer problems, to which we add those of the interface condition:

$$\begin{aligned}
\frac{\partial \mathcal{J}}{\partial (\mathbf{u}, p)} \delta (\mathbf{u}, p) = & \\
& \oint_{\Gamma_{\text{int}}} \Sigma_{ij} (\delta p^-, \delta \mathbf{u}^-) n_j \left(2\delta_{i1} - u_i^{\dagger-} + u_k^{\dagger\dagger} Re \mathcal{M}_{ki} \right) \\
& + \left(\Sigma_{ij} (-p^{\dagger-}, \mathbf{u}^{\dagger-}) n_j + U_k n_k u_i^{\dagger-} - u_i^{\dagger\dagger} \right) \delta u_i^- d\Gamma \\
& - \oint_{\Gamma_{\text{int}}} \Sigma_{ij} (\delta p^+, \delta \mathbf{u}^+) n_j \left(2\delta_{i1} - u_i^{\dagger+} + u_k^{\dagger\dagger} Re \mathcal{M}_{ki} \right) \\
993 & + \left(\Sigma_{ij} (-p^{\dagger+}, \mathbf{u}^{\dagger+}) n_j + (U_k n_k) u_i^{\dagger+} \right) \delta u_i^+ d\Gamma & (B 8) \\
& + \oint_{\partial\Omega} -\Sigma_{ij} (\delta p, \delta \mathbf{u}) n_j u_i^\dagger + \left(\Sigma_{ij} (-p^\dagger, \mathbf{u}^\dagger) n_j + U_k n_k u_i^\dagger \right) \delta u_i d\Gamma \\
& + \int_{\Omega} \partial_i u_i^\dagger \delta p \, d\Omega \\
& - \int_{\Omega} u_j^\dagger \partial_i U_j - U_j \partial_j u_i^\dagger - \partial_i p^\dagger - \frac{1}{Re} \partial_{jj}^2 u_i^\dagger \delta u_i \, d\Omega
\end{aligned}$$

994 Exploiting the relation $\delta \mathbf{u} = \delta \mathbf{u}^+ = \delta \mathbf{u}^-$, canceling the surface term on Ω and the boundary
995 terms on Γ_{int} and $\partial\Omega$, we define $(\mathbf{u}^\dagger, p^\dagger)$ as the solution to the adjoint linear equations

$$\begin{aligned}
& \partial_i u_i^\dagger = 0, \quad u_j^\dagger \partial_i U_j - U_j \partial_j u_i^\dagger = \partial_i p^\dagger + \frac{1}{Re} \partial_{jj}^2 u_i^\dagger \quad \text{in } \Omega \\
996 & \left(\Sigma_{ik} (-p^{\dagger-}, \mathbf{u}^{\dagger-}) - \Sigma_{ik} (-p^{\dagger+}, \mathbf{u}^{\dagger+}) \right) n_k - u_i^{\dagger\dagger} = 0 \quad \text{on } \Gamma_{\text{int}} & (B 9) \\
& u_i^{\dagger+} = u_i^{\dagger-} \quad \text{on } \Gamma_{\text{int}}
\end{aligned}$$

997 with

$$998 \quad u_i^{\dagger\dagger} = Re^{-1} \mathcal{M}_{ji}^{-1} \left(u_j^{\dagger-} - 2\delta_{1j} \right) \quad \text{on } \Gamma_{\text{int}}, \quad (B 10)$$

999 together with adjoint boundary conditions $\mathbf{u}^\dagger = 0$ at the inflow and $\Sigma_{ik} (-p^\dagger, \mathbf{u}^\dagger) n_k +$

1000 $U_k n_k u_i^\dagger = 0$ at the outflow and lateral boundaries of the domain Γ_{lat} . We thus have:

$$1001 \quad \delta C_D = \frac{\partial \mathcal{J}}{\partial \mathcal{M}_{ij}} \delta \mathcal{M}_{ij} = \oint_{\Gamma_{\text{int}}} u_i^{\dagger\dagger} \text{Re} \delta \mathcal{M}_{ij} (\Sigma_{jk}(P^-, U^-) - \Sigma_{jk}(P^+, U^+)) n_k \, d\Gamma. \quad (\text{B } 11)$$

1002 Since $\mathcal{M}_{ij} = \mathcal{L} t_i t_j - \mathcal{F} n_i n_j$, we are able to evaluate the sensitivities with respect to \mathcal{F} and
1003 \mathcal{L} separately. Specializing equation (B 11) for \mathcal{F} we obtain

$$1004 \quad \delta C_D = \frac{\partial \mathcal{J}}{\partial \mathcal{F}} \delta \mathcal{F} = - \oint_{\Gamma_{\text{int}}} u_i^{\dagger\dagger} \text{Re} \delta \mathcal{F} n_i n_j (\Sigma_{jk}(P^-, U^-) - \Sigma_{jk}(P^+, U^+)) n_k \, d\Gamma. \quad (\text{B } 12)$$

1005 The sensitivity with respect to \mathcal{F} thus reads

$$1006 \quad \nabla_{\mathcal{F}} C_D = -\text{Re} u_i^{\dagger\dagger} n_i n_j (\Sigma_{jk}(P^-, U^-) - \Sigma_{jk}(P^+, U^+)) n_k, \quad (\text{B } 13)$$

1007 while, applying the same procedure with respect to \mathcal{L} , we obtain

$$1008 \quad \nabla_{\mathcal{L}} C_D = \text{Re} u_i^{\dagger\dagger} t_i t_j (\Sigma_{jk}(P^-, U^-) - \Sigma_{jk}(P^+, U^+)) n_k. \quad (\text{B } 14)$$

1009 It is finally clear that the gradients of C_D can be evaluated only if the solution of the adjoint
1010 problem B 9 is known. As a matter of example, in figure 27 we report the adjoint fields
1011 ($\mathbf{u}^\dagger, p^\dagger, \mathbf{u}^{\dagger\dagger}$) for $Re = 100$, $\mathcal{F} = 1.25 \times 10^{-2}$ and $\mathcal{L} = 5 \times 10^{-3}$.

1012 Appendix C. Geometrical data associated with the full-scale structures analyzed 1013 in Section 6

1014 In Section 6 different full-scale geometries with arbitrary varying solid inclusions have been
1015 proposed. Table 3 lists the parameter needed to build the cylindrical shell for each case.
1016 Distributions D1 and D2 correspond to test cases 1 and 2 that leads to the profiles of \mathcal{F}
1017 and \mathcal{L} depicted in panels *b*) and *c*) of figure 22, while distributions D3 and D4 correspond
1018 to the optimal full-scale structures found in Section 6.2 with ϵ equal to 0.1369 and 0.0667,
1019 respectively. Each entry of the table contains the value of the radius of the i -th circular solid
1020 inclusion, normalized by ℓ . The i -th inclusion is positioned at an angle $\alpha = \frac{2\pi}{N}(i-1)$ where
1021 $N = 23$ for distributions D1, D2, D3 and $N = 47$ for distribution D4. To have a visual idea of
1022 which kind of structures we are dealing with, in figure 28 a visualization of the corresponding
1023 full-scale membrane geometries is represented for the distributions listed in table 3.

1024 For the sake of clarity we list the main steps of the bisection algorithm used to reconstruct
1025 the inclusions' distributions D3 and D4 listed in table 3. We denote with $R_i^{(m)}$ the radius
1026 of the i -th inclusion forming the membrane, adimensionalized with the microscopic length,
1027 according to table 3. The superscript (m) is used here to denote the m -th iteration of the
1028 bisection method.

1029 • two initial guess values are taken respectively equal to $R_i^{per} - \epsilon R_i^{per}$ and $R_i^{per} + \epsilon R_i^{per}$
1030 where R^{per} is the radius of the inclusion which realizes the value \mathcal{F}_i^{opt} as if the lattice was
1031 periodic, with \mathcal{F}_i^{opt} the optimal filtrability evaluated in the i -th cell;

1032 • at each iteration (m) and for every i the quantity $\mathcal{F}_i^{(m)}$ is evaluated by solving the
1033 microscopic problem (4.1) on the whole cylinder as explained in Section 6;

1034 • if $\mathcal{F}_i^{(m)} - \mathcal{F}_i^{opt} < 0$ the radius of the i -th inclusion at iteration (m) is decreased of a
1035 quantity $0.5|R_i^{(m)} - R_i^{(m-1)}|$;

1036 • if $\mathcal{F}_i^{(m)} - \mathcal{F}_i^{opt} > 0$ the radius of the i -th inclusion at iteration (m) is increased of a
1037 quantity $0.5|R_i^{(m)} - R_i^{(m-1)}|$;

1038 • the procedure is repeated until convergence, i.e. when $|\mathcal{F}_i^{(n)} - \mathcal{F}_i^{opt}|/|\mathcal{F}_i^{opt}| < \text{tol}$,
1039 where $\text{tol} = 0.01$.

i	D1	D2	D3	D4
1	0.10	0.10	0.070	0.0300
2	0.11	0.40	0.130	0.0320
3	0.12	0.12	0.280	0.0750
4	0.13	0.40	0.370	0.1170
5	0.14	0.14	0.090	0.2100
6	0.15	0.40	0.043	0.2750
7	0.16	0.40	0.050	0.3000
8	0.17	0.17	0.050	0.2300
9	0.19	0.40	0.390	0.0550
10	0.20	0.19	0.015	0.0150
11	0.22	0.40	0.063	0.0090
12	0.23	0.22	0.062	0.0135
13	0.22	0.40	0.062	0.0140
14	0.20	0.22	0.063	0.0110
15	0.19	0.40	0.015	0.0060
16	0.18	0.19	0.390	0.0500
17	0.17	0.40	0.050	0.3200
18	0.16	0.17	0.050	0.3300
19	0.15	0.40	0.043	0.0008
20	0.14	0.15	0.090	0.0085
21	0.13	0.40	0.370	0.0132
22	0.12	0.13	0.280	0.0149
23	0.11	0.40	0.130	0.0160
24	–	–	–	0.0160

Table 3: Values of the radius of the i -th solid inclusion, adimensionalized with the microscopic length, for $i = 1, \dots, 24$ for distributions D1, D2, D3 and D4. Please notice that, in distribution D4, 47 solid inclusions are present and the radius of the j -th inclusion for $j = 25, \dots, 47$ is equal to the radius of the i -th inclusion, satisfying the formula $j = 47 - i + 1$.

REFERENCES

- 1040 ABDERRAHAMAN-ELENA, N. & GARCÍA-MAYORAL, R. 2017 Analysis of anisotropically permeable surfaces
1041 for turbulent drag reduction. *Physical Review Fluids* **2** (11), 114609.
- 1042 ASADZADEH, S.S., NIELSEN, LASSE T., ANDERSEN, A., DÖLGER, J., KIØRBOE, T., LARSEN, P.S. & WALTHER,
1043 J.H. 2019 Hydrodynamic functionality of the lorica in choanoflagellates. *Journal of The Royal Society*
1044 *Interface* **16** (150), 20180478.
- 1045 BADDOO, PETER J, HAJIAN, ROZHIN & JAWORSKI, JUSTIN W 2021 Unsteady aerodynamics of porous aerofoils.
1046 *Journal of Fluid Mechanics* **913**.
- 1047 BARKLEY, D. 2006 Linear analysis of the cylinder wake mean flow. *Europhysics Letters* **75** (5), 750–756.
- 1048 BARKLEY, D. & HENDERSON, R.D. 1996 Three-dimensional floquet stability analysis of the wake of a circular
1049 cylinder. *Journal of Fluid Mechanics* **322**, 215–241.
- 1050 BARTA, E. & WEIHS, D. 2006 Creeping flow around a finite row of slender bodies in close proximity. *Journal*
1051 *of Fluid Mechanics* **551**, 1–17.
- 1052 BONGARZONE, A., BERTSCH, A., RENAUD, P. & GALLAIRE, F. 2021 Impinging planar jets: hysteretic behaviour
1053 and origin of the self-sustained oscillations. *Journal of Fluid Mechanics* **913**, A51.
- 1054 BOUJO, E., EHRENSTEIN, U. & GALLAIRE, F. 2013 Open-loop control of noise amplification in a separated
1055 boundary layer flow. *Physics of Fluids* **25** (12), 124106.
- 1056 BOUJO, E. & GALLAIRE, F. 2014 Controlled reattachment in separated flows: a variational approach to
1057 recirculation length reduction. *Journal of Fluid Mechanics* **742**, 618–635.
- 1058 BOUJO, E. & GALLAIRE, F. 2015 Sensitivity and open-loop control of stochastic response in a noise amplifier
1059 flow: the backward-facing step. *Journal of Fluid Mechanics* **762**, 361–392.
- 1060 BRINKMAN, H. C. 1949 A calculation of the viscous force exerted by a flowing fluid on a dense swarm of
1061 particles. *Flow, Turbulence and Combustion* **1** (1), 27.

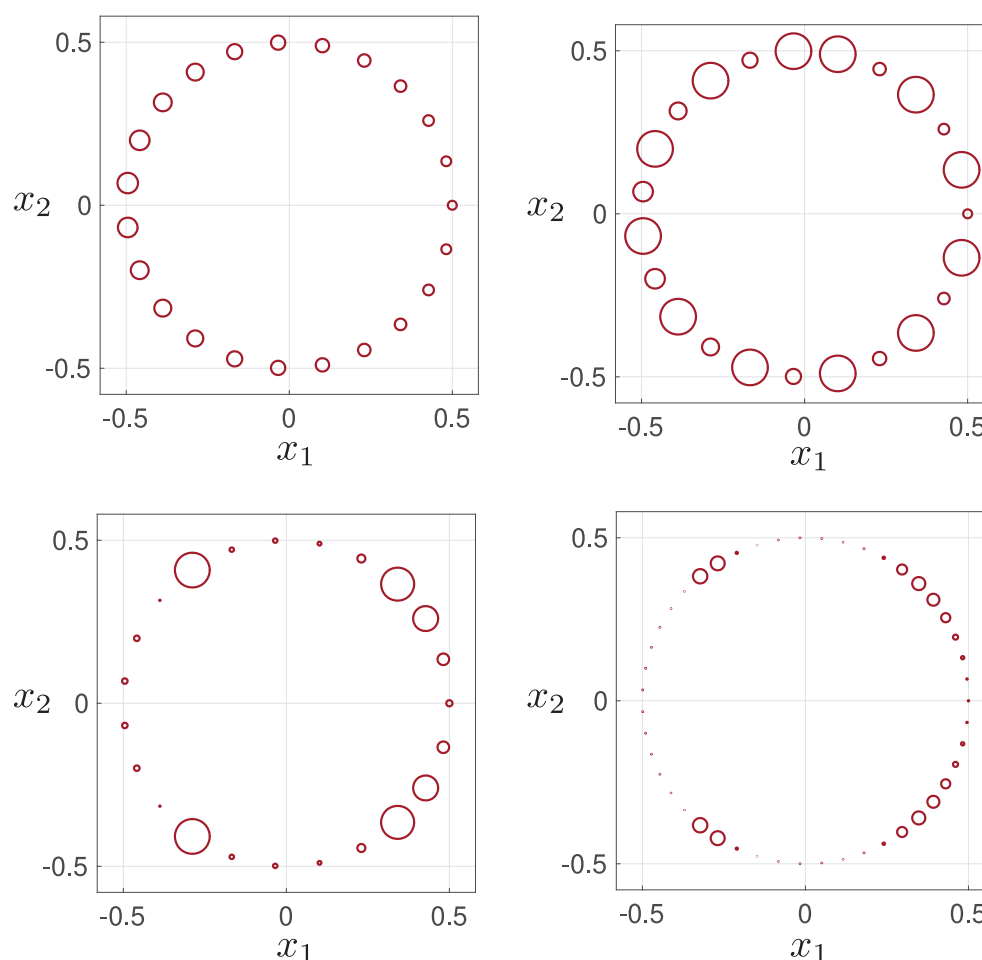


Figure 28: Visualization of the whole full-scale membrane geometry for configurations D1, D2, D3 and D4 in lexicographic order.

- 1062 CAMARRI, S. & IOLLO, A. 2010 Feedback control of the vortex-shedding instability based on sensitivity
1063 analysis. *Physics of Fluids* **22** (9), 094102.
- 1064 CASTRO, I. P. 1971 Wake characteristics of two-dimensional perforated plates normal to an air-stream.
1065 *Journal of Fluid Mechanics* **46** (3), 599–609.
- 1066 CHOMAZ, J-M 2005 Global instabilities in spatially developing flows: Non-normality and nonlinearity.
1067 *Annual Review of Fluid Mechanics* **37** (1), 357–392.
- 1068 CRABILL, J., WITHERDEN, F.D. & JAMESON, A. 2018 A parallel direct cut algorithm for high-order overset
1069 methods with application to a spinning golf ball. *Journal of Computational Physics* **374**, 692–723.
- 1070 CUMMINS, C., SEALE, M., MACENTE, A., CERTINI, D., MASTROPAOLO, E., VIOLA, I.M. & NAKAYAMA, N.
1071 2018 A separated vortex ring underlies the flight of the dandelion. *Nature* **562** (7727), 414–418.
- 1072 CUMMINS, C., VIOLA, I.M., MASTROPAOLO, E. & NAKAYAMA, N. 2017 The effect of permeability on the flow
1073 past permeable disks at low Reynolds numbers. *Physics of Fluids* **29** (9).
- 1074 DALWADI, M. P., BRUNA, M. & GRIFFITHS, I. M. 2016 A multiscale method to calculate filter blockage.
1075 *Journal of Fluid Mechanics* **809**, 264–289.
- 1076 DARCY, H. 1856 *Les fontaines publiques de la ville de Dijon: exposition et application des principes a suivre*
1077 *et des formules a employer dans les questions de distribution d'eau*. Paris: Victor Dalmont.
- 1078 ELIMELECH, M. & PHILLIP, W. 2011 The future of seawater desalination: Energy, technology, and the
1079 environment. *Science* **333**, 712–717.
- 1080 ELLINGTON, C.P. 1980 Wing mechanics and take-off preparation of thrips (thysanoptera). *Journal of*
1081 *Experimental Biology* **85** (1), 129–136.
- 1082 FORNBERG, B. 1980 A numerical study of steady viscous flow past a circular cylinder. *Journal of Fluid*
1083 *Mechanics* **98** (4), 819–855.
- 1084 FRITZMANN, C., LOWENBERG, J., WINTGENS, T. & MELIN, T. 2007 State-of-the-art of reverse osmosis
1085 desalination. *Desalin.* **216**, 1–76.

- 1086 GARCIA-MAYORAL, R. & JIMÉNEZ, J. 2011 Drag reduction by riblets. *Philosophical transactions of the Royal*
1087 *society A: Mathematical, physical and engineering Sciences* **369** (1940), 1412–1427.
- 1088 GIANNETTI, F. & LUCHINI, P. 2007 Structural sensitivity of the first instability of the cylinder wake. *Journal*
1089 *of Fluid Mechanics* **581**, 167–197.
- 1090 HAJIAN, ROZHIN & JAWORSKI, JUSTIN W 2017 The steady aerodynamics of aerofoils with porosity gradients.
1091 *Proceedings of the Royal Society A: Mathematical, Physical and Engineering Sciences* **473** (2205),
1092 20170266.
- 1093 HORNUNG, U. 1997 *Homogenization and Porous Media*. New York: Springer.
- 1094 ICARDI, M., BOCCARDO, G., MARCHISIO, D.L., TOSCO, T. & SETHI, R. 2014 Pore-scale simulation of fluid
1095 flow and solute dispersion in three-dimensional porous media. *Phys. Rev. E* **90**, 013032.
- 1096 IUNGO, G.V., VIOLA, F., CAMARRI, S., PORTÉ-AGEL, F. & GALLAIRE, F. 2013 Linear stability analysis of wind
1097 turbine wakes performed on wind tunnel measurements. *Journal of Fluid Mechanics* **737**, 499–526.
- 1098 JACKSON, C.P. 1987 A finite-element study of the onset of vortex shedding in flow past variously shaped
1099 bodies. *Journal of fluid Mechanics* **182**, 23–45.
- 1100 JAWORSKI, J.W. & PEAKE, N. 2020 Aeroacoustics of silent owl flight. *Annual Review of Fluid Mechanics*
1101 **52** (1), 395–420.
- 1102 JENSEN, K. H., BERG-SØRENSEN, K., BRUUS, H., HOLBROOK, N.M., LIESCHE, J., SCHULZ, A., ZWIENIECKI,
1103 M.A. & BOHR, T. 2016 Sap flow and sugar transport in plants. *Rev. Mod. Phys.* **88** (035007).
- 1104 JONES, S.K., YUN, Y.J.J., HEDRICK, T.L., GRIFFITH, B.E. & MILLER, L.A. 2016 Bristles reduce the force
1105 required to ‘fling’ wings apart in the smallest insects. *Journal of Experimental Biology* **219** (23),
1106 3759–3772.
- 1107 LABBÉ, R & DUPRAT, C 2019 Capturing aerosol droplets with fibers. *Soft Matter* **15** (35), 6946–6951.
- 1108 LĀCIS, U. & BAGHERI, S. 2017 A framework for computing effective boundary conditions at the interface
1109 between free fluid and a porous medium. *J. Fluid Mech.* **812**, 866–889.
- 1110 LĀCIS, U., ZAMPOGNA, G.A. & BAGHERI, S. 2017 A computational continuum model of poroelastic beds.
1111 *Proceedings of the Royal Society A: Mathematical, Physical and Engineering Sciences* **473** (2199),
1112 20160932.
- 1113 LĀCIS, U., SUDHAKAR, Y., PASCHE, S. & BAGHERI, S. 2020 Transfer of mass and momentum at rough and
1114 porous surfaces. *Journal of Fluid Mechanics* **884**, A21.
- 1115 LEDDA, P. G., SICONOLFI, L., VIOLA, F., CAMARRI, S. & GALLAIRE, F. 2019 Flow dynamics of a dandelion
1116 pappus: A linear stability approach. *Phys. Rev. Fluids* **4**, 071901.
- 1117 LEDDA, P. G., SICONOLFI, L., VIOLA, F., GALLAIRE, F. & CAMARRI, S. 2018 Suppression of von kármán
1118 vortex streets past porous rectangular cylinders. *Phys. Rev. Fluids* **3**, 103901.
- 1119 LEMKE, M., REISS, J. & SESTERHENN, J. 2014 Adjoint based optimisation of reactive compressible flows.
1120 *Combustion and Flame* **161** (10), 2552–2564.
- 1121 LIN, CHIH-JEN 2007 Projected gradient methods for nonnegative matrix factorization. *Neural computation*
1122 **19** (10), 2756–2779.
- 1123 LUCHINI, P. & BOTTARO, A. 2014 Adjoint equations in stability analysis. *Annual Review of Fluid Mechanics*
1124 **46** (1), 493–517.
- 1125 MARQUET, O., SIPP, D. & JACQUIN, L. 2008 Sensitivity analysis and passive control of cylinder flow. *Journal*
1126 *of Fluid Mechanics* **615**, 221.
- 1127 MATIN, A., KHAN, Z., ZAIDIA, S. M. J. & BOYCE, M. C. 2011 Biofouling in reverse osmosis membranes for
1128 seawater desalination: Phenomena and prevention. *Desalin.* **281**, 1–16.
- 1129 MELIGA, P., BOUJO, E., PUJALS, G. & GALLAIRE, F. 2014 Sensitivity of aerodynamic forces in laminar and
1130 turbulent flow past a square cylinder. *Physics of Fluids* **26** (10), 104101.
- 1131 MELIGA, P., CHOMAZ, J.-M. & SIPP, D. 2009 Unsteadiness in the wake of disks and spheres: Instability,
1132 receptivity and control using direct and adjoint global stability analyses. *Journal of Fluids and*
1133 *Structures* **25** (4), 601–616.
- 1134 MELIGA, P., SIPP, D. & CHOMAZ, J.-M 2010 Open-loop control of compressible afterbody flows using adjoint
1135 methods. *Physics of Fluids* **22** (5), 054109.
- 1136 MONKEWITZ, P.A. 1988 The absolute and convective nature of instability in two dimensional wakes at low
1137 reynolds numbers. *The Physics of Fluids* **31** (5), 999–1006.
- 1138 NEMILI, A., ÖZKAYA, E., GAUGER, N., THIELE, F. & CARNARIUS, A. 2011 Optimal control of unsteady flows
1139 using discrete adjoints. In *41st AIAA Fluid Dynamics conference and exhibit*, p. 3720.
- 1140 NICOLLE, A. & EAMES, I. 2011 Numerical study of flow through and around a circular array of cylinders.
1141 *Journal of Fluid Mechanics* **679**, 1–31.

- 1142 NORBERG, C. 2003 Fluctuating lift on a circular cylinder: review and new measurements. *Journal of Fluids*
1143 *and Structures* **17** (1), 57–96.
- 1144 OLIVIER, J. 2004 Fog harvesting: An alternative source of water supply on the west coast of south africa.
1145 *GeoJournal* **61** (2), 203–214.
- 1146 PARK, H. B., KAMCEV, J., ROBESON, L. M., ELIMELECH, M. & FREEMAN, B. D. 2017 Maximizing the right
1147 stuff: the trade-off between membrane permeability and selectivity. *Science* **356** (6343).
- 1148 PARK, K-C, CHHATRE, S.S., SRINIVASAN, S., COHEN, R.E. & MCKINLEY, G.H. 2013 Optimal design of
1149 permeable fiber network structures for fog harvesting. *Langmuir* **29** (43), 13269–13277.
- 1150 PASCHE, S., AVELLAN, F. & GALLAIRE, F. 2017 Part load vortex rope as a global unstable mode. *Journal of*
1151 *Fluids Engineering* **139** (5).
- 1152 PEZZULLA, M., STRONG, E. F., GALLAIRE, F. & REIS, P. M. 2020 Deformation of porous flexible strip in low
1153 and moderate reynolds number flows. *Phys. Rev. Fluids* **5**, 084103.
- 1154 PROVANSAL, M., MATHIS, C. & BOYER, L. 1987 Bénard-von kármán instability: transient and forced regimes.
1155 *Journal of Fluid Mechanics* **182**, 1–22.
- 1156 QUARTERONI, ALFIO 2017 *Domain decomposition methods*, pp. 555–612. Cham: Springer International
1157 Publishing.
- 1158 RAHARDIANTO, A., MCCOOL, B. C. & COHEN, Y. 2010 Accelerated desupersaturation of reverse osmosis
1159 concentrate by chemically-enhanced seeded precipitation. *Desalin.* **264**, 256–267.
- 1160 SCHULZE, J. & SESTERHENN, J. 2013 Optimal distribution of porous media to reduce trailing edge noise.
1161 *Computers & Fluids* **78**, 41–53, IES of turbulence aeroacoustics and combustion.
- 1162 GÓMEZ-DE SEGURA, G. & GARCÍA-MAYORAL, R. 2019 Turbulent drag reduction by anisotropic permeable
1163 substrates – analysis and direct numerical simulations. *Journal of Fluid Mechanics* **875**, 124–172.
- 1164 SHANNON, M. A., BOHN, P. W., ELIMELECH, M., GEORGIADIS, J. G., MARIÑAS, B. J. & MAYES, A. M. 2008
1165 Science and technology for water purification in the coming decades. *Nature* **452**, 301–310.
- 1166 SHI, W., ANDERSON, M.J., TULKOFF, J.B., KENNEDY, B.S. & BOREYKO, J.B. 2018 Fog harvesting with harps.
1167 *ACS applied materials & interfaces* **10** (14), 11979–11986.
- 1168 STEIROS, K. & HULTMARK, M. 2018 Drag on flat plates of arbitrary porosity. *Journal of Fluid Mechanics*
1169 **853**, R3.
- 1170 STEIROS, K., KOKMANIAN, K., BEMPEDELIS, N. & HULTMARK, M. 2020 The effect of porosity on the drag of
1171 cylinders. *J. Fluid Mech* **901**, R2.
- 1172 STRONG, E. F., PEZZULLA, M., GALLAIRE, F., REIS, P. & SICONOLFI, L. 2019 Hydrodynamic loading of
1173 perforated disks in creeping flows. *Phys. Rev. Fluids* **4**, 084101.
- 1174 THEOFILIS, V. 2011 Global linear instability. *Annual Review of Fluid Mechanics* **43** (1), 319–352.
- 1175 VIOLA, F., IUNGO, G. V., CAMARRI, S., PORTÉ-AGEL, F. & GALLAIRE, F. 2014 Prediction of the hub vortex
1176 instability in a wind turbine wake: stability analysis with eddy-viscosity models calibrated on wind
1177 tunnel data. *Journal of Fluid Mechanics* **750**, R1.
- 1178 WAGNER, H., WEGER, M., KLAAS, M. & SCHRÖDER, W. 2017 Features of owl wings that promote silent
1179 flight. *Interface Focus* **7** (1), 20160078.
- 1180 WILLERT, C., SCHULZE, M., WALTENS PÜL, S., SCHANZ, D. & KOMPENHANS, J. 2019 Prandtl’s flow
1181 visualization film c1 revisited. *13th Int. Symp. on Particle Image Velocimetry*, arXiv: https://elib.dlr.de/128984/1/ISPIV2019_Willert_Paper161.pdf.
- 1183 WILLIAMSON, C. H. K. 1996 Vortex dynamics in the cylinder wake. *Annual Review of Fluid Mechanics*
1184 **28** (1), 477–539.
- 1185 ZAMPOGNA, G.A. & GALLAIRE, F. 2020 Effective stress jump across membranes. *Journal of Fluid Mechanics*
1186 **892**, A9.
- 1187 ZAMPOGNA, G.A., PLUVINAGE, F., KOURTA, A. & BOTTARO, A. 2016 Instability of canopy flows. *Water*
1188 *Resources Research* **52** (7), 5421–5432.
- 1189 ZAMPOGNA, G. A. & BOTTARO, A. 2016 Fluid flow over and through a regular bundle of rigid fibres. *Journal*
1190 *of Fluid Mechanics* **792**, 5–35.
- 1191 ZAMPOGNA, G. A., MAGNAUDET, J. & BOTTARO, A. 2019 Generalized slip condition over rough surfaces.
1192 *Journal of Fluid Mechanics* **858**, 407–436.
- 1193 ZONG, L. & NEPF, H. 2012 Vortex development behind a finite porous obstruction in a channel. *Journal of*
1194 *Fluid Mechanics* **691**, 368–391.